THE JOURNAL OF PHYSICAL CHEMISTRY B

Article

pubs.acs.org/JPCB

Precision Measurements of Deuterium Isotope Effects on the Chemical Shifts of Backbone Nuclei in Proteins: Correlations with Secondary Structure

Hechao Sun[†] and Vitali Tugarinov*[,†]

[†]Department of Chemistry and Biochemistry, University of Maryland, College Park, Maryland 20742, United States

Supporting Information

ABSTRACT: Precision NMR measurements of deuterium isotope effects on the chemical shifts of backbone nuclei in proteins (^{15}N, ^{13}CO, $^{13}C_{\alpha}$, and ^{1}HN) arising from ^{1}H-to-^{2}H substitutions at aliphatic carbon sites. Isolation of molecular species with a defined protonation/deuteration pattern at carbon-α/β positions allows distinguishing and accurately quantifying different isotope effects within the protein backbone. The isotope shifts measured in the partially deuterated protein ubiquitin are interpreted in terms of backbone geometry via empirical relationships describing the dependence of isotope shifts on $(\varphi; \psi)$ backbone dihedral angles. Because of their relatively large magnitude and clear dependence on the protein secondary structure, the two- and three-bond backbone amide ^{15}N isotope shifts, $^{2}\Delta N(C_{\alpha,i}D)$ and $^{3}\Delta N(C_{\alpha,i-1}D)$, can find utility for NMR structural refinement of small-to-medium size proteins.

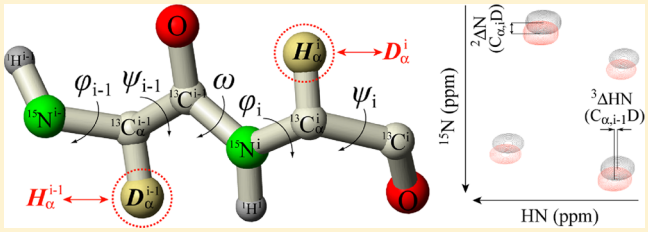

INTRODUCTION

Deuteration of protein molecules at nonexchangeable carbon sites has found widespread use in solution NMR applications.[1−6] Despite the fact that the number of proton nuclear probes available for NOE-based structure determination is severely reduced at high levels of deuteration, longer relaxation times of ^{13}C nuclei allow detailed NMR characterization of high-molecular-weight proteins via more effective use of the remaining exchangeable amide protons (^{1}HN)[7−11] and/or selectively back-protonated methyl ($^{13}CH_3$) sites.[6,12−16] One of the consequences of incorporation of deuterium into nonexchangeable backbone and side-chain positions of proteins is the change in the isotropic chemical shifts of nuclei removed up to four bonds away from the deuteration site - deuterium isotope shifts.[17,18]

Although the importance of these effects in small organic compounds was recognized more than two decades ago,[18−20] the vast majority of quantitative NMR studies of isotope effects in peptides and proteins concentrated on the effects of protium-to-deuterium substitution at exchangeable sites (amide, NH→ND, tyrosine hydroxyl, OH→OD, or cysteine sulfhydryl, SH→SD, groups). The measurements of isotope shifts of carbonyl carbons in peptides and proteins,[21−26] protein backbone $^{13}C_{\alpha}$ nuclei,[27,28] and side-chain $^{13}C_{\beta}$ sites[29] as well as Tyr ring $^{13}C_{\zeta}$[30] and Cys $^{13}C_{\beta}$ positions[31] have been reported. The effects of hydrogen-bonding on ^{15}N shifts resulting from NH→ND substitutions in the backbone[32] and side-chain[33] amides have been analyzed. Deuterium isotope effects on trans-hydrogen bond scalar couplings have been related to the hydrogen-bond strength.[34]

The effects of ^{1}H-to-D substitutions at nonexchangeable sites of proteins on ^{15}N and ^{13}C chemical shifts is more difficult to quantify accurately because these substitutions are commonly made at all carbon sites simultaneously. The effects of multiple ^{1}H-to-D replacements are cumulative, and it is difficult to disentangle the contributions of multiple replacements to the isotope shift of a particular nucleus. In fact, such deuterium isotope shifts are usually viewed as a nuisance because they may complicate assignments of NMR resonances[35−38] and, in the case of incomplete deuteration, also broaden ^{13}C line widths.[27] With only one notable exception,[39] these isotope effects have been commonly quantified from comparisons of chemical shifts in fully protonated and fully deuterated protein molecules,[14,27,35,36,40] leading to quite crude estimates that likely overestimate the magnitude of isotope shifts. However, the knowledge of their accurate values and improved understanding of their physical origins can turn deuterium isotope shifts into useful reporters of protein backbone and side-chain geometry.

Here, we describe precision NMR measurements of deuterium isotope effects on the chemical shifts of protein backbone nuclei ($^{13}C_{\alpha}$, ^{15}N, ^{13}CO, and ^{1}HN) arising from ^{1}H-to-D substitutions at nonexchangeable sites - primarily, backbone C_{α} positions. Isolation of molecular species with defined labeling (protonation/deuteration) patterns at successive C_{α} sites allows distinguishing and accurately quantifying different isotope effects within the protein backbone. The

Received: May 3, 2012
Revised: June 7, 2012
Published: June 8, 2012

dx.doi.org/10.1021/jp304300n | J. Phys. Chem. B 2012, 116, 7436−7448

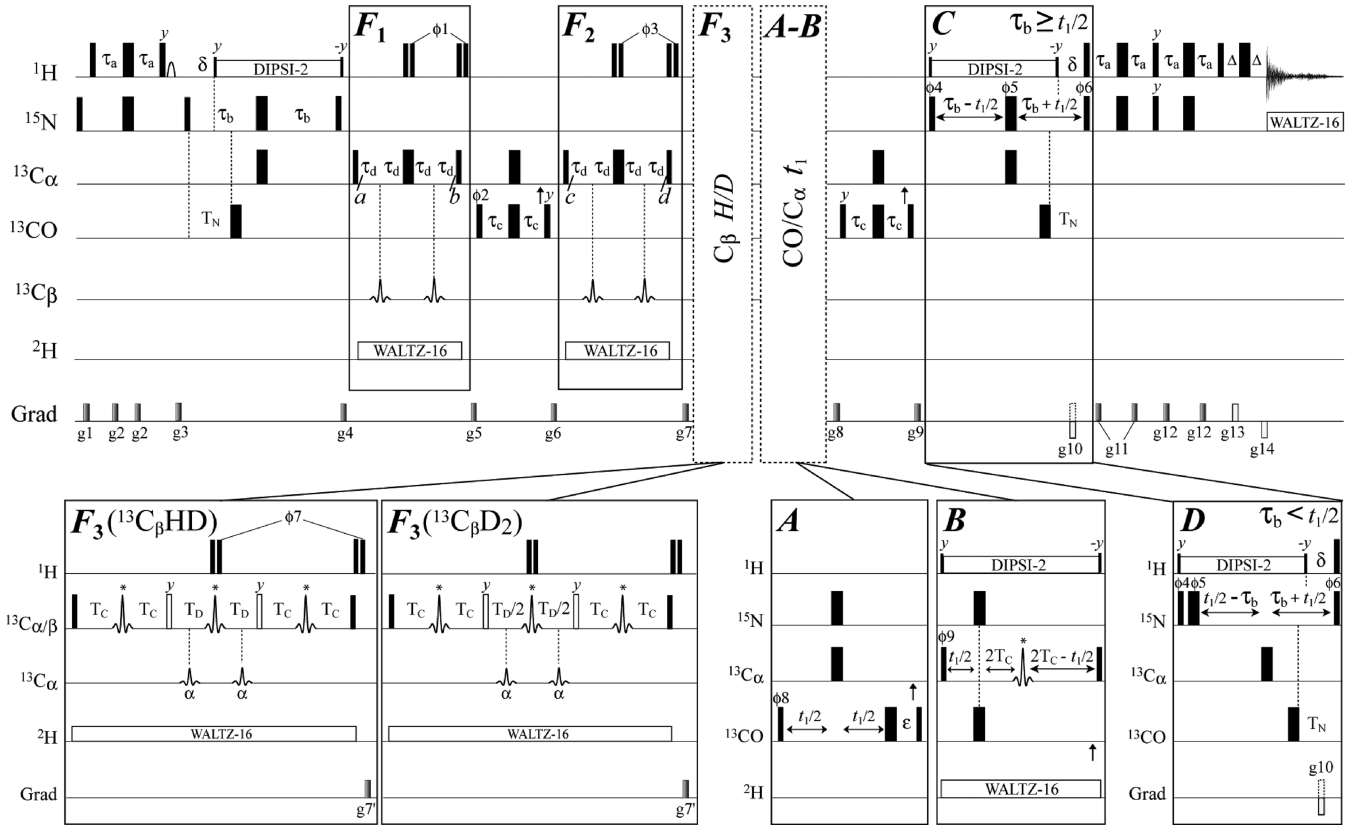

Figure 1. 2D *intra*-HN[CA/CO] pulse-scheme for the measurement of deuterium isotope effects on the chemical shifts of backbone ^{15}N, ^{1}HN, ^{13}CO, and ^{13}C$^{\alpha}$ nuclei of proteins. See 'Materials and Methods' for experimental details.

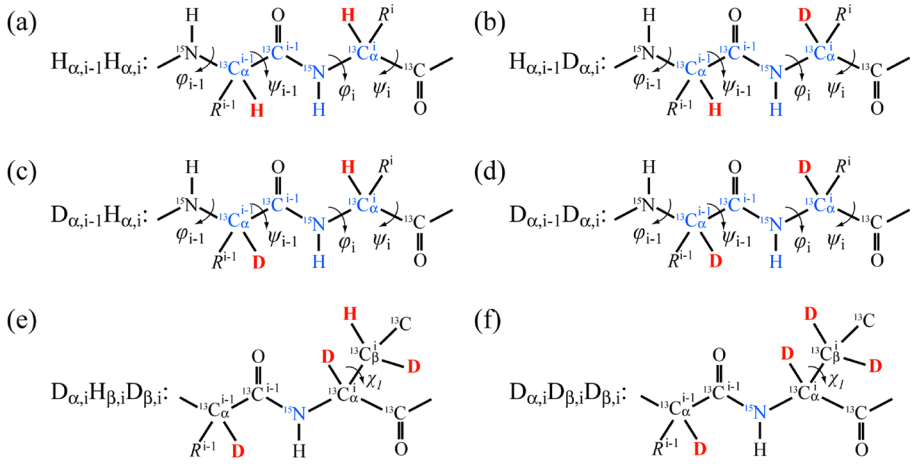

Figure 2. Schematic representation of dipeptide fragments in various states of protonation/deuteration at α/β positions. The nuclei whose isotope shifts have been measured in this work are shown in blue, while the sites of proton-to-deuterium substitution are indicated in red. The torsion angles of residues i and i-1 are indicated with arrows. Double-filtering achieved by the elements F_1 and F_2 of the scheme in Figure 1 ensures isolation of NMR signals corresponding to each type of molecular species: (**a**) $H_{\alpha,i-1}H_{\alpha,i}$; (**b**) $H_{\alpha,i-1}D_{\alpha,i}$; (**c**) $D_{\alpha,i-1}H_{\alpha,i}$; and (**d**) $D_{\alpha,i-1}D_{\alpha,i}$. Additional filtering F_3 (Figure 1) can be used to separate the molecular species with either CHD or CD_2 groups at β positions. Two types of F_3 filtering have been used resulting in isolation of molecular species of (**e**) $D_{\alpha,i}H_{\beta,i}D_{\beta,i}$ and (**f**) $D_{\alpha,i}D_{\beta,i}D_{\beta,i}$ variety for the measurements of isotope effects of a single β proton-to-deuterium ($^{1}H^{\beta}\rightarrow D^{\beta}$) substitution on ^{15}N chemical shifts.

dependence of the magnitude of isotope effects on a variety of factors, many of which remain poorly understood, necessitates the use of an empirical treatment - similar to the approach used for interpretation of $^{13}C_{\alpha}$ isotope shifts arising from the backbone amide NH→ND substitutions by Ottiger and Bax.[27] The isotope effects measured in the partially deuterated protein ubiquitin are interpreted in terms of backbone geometry via empirical relationships describing the dependence of isotope shifts on (φ; ψ) dihedral angles. The utility of the measured isotope shifts as reporters of backbone geometry lies mainly in the observed Karplus-type relationships of the three-bond effects on the backbone dihedral angles formed by the three intervening bonds - in agreement with earlier observations.[20,26,41,42] Because of their relatively large magnitude and

dx.doi.org/10.1021/jp304300n | J. Phys. Chem. B 2012, 116, 7436−7448

dependence on the backbone geometry, the two- and three-bond ^{15}N isotope shifts, $^{2}\Delta N(C_{\alpha,i}D)$ and $^{3}\Delta N(C_{\alpha,i-1}D)$, may prove potentially useful for NMR structural refinement of small-to-medium size proteins.

MATERIALS AND METHODS

NMR Sample. The sample of [U-^{15}N; ^{13}C]-labeled wild-type human ubiquitin (pdb code -1ubq[43]) used in this work was ~60% deuterated. This deuteration level has been achieved by the use of [U-^{1}H,^{13}C]-glucose as the main carbon source in 60%D_2O/40%H_2O M9 minimal medium. As carbon-α sites of the protein backbone acquire the attached protons/deuterons primarily from the solvent of the medium,[12−14] this results in approximately 60% deuteration at α positions. This level of deuteration at α-sites has been confirmed experimentally from the ratios of peak intensities obtained in NMR spectra acquired with different $^{13}C_\alpha H_\alpha/^{13}C_\alpha D_\alpha$ filtering schemes (see text). The [U-^{15}N,^{13}C, 60%-^{2}H/40%-^{1}H]-labeled NMR sample was 3.0 mM in protein concentration and dissolved in a 20 mM 90% H_2O/10% D_2O sodium phosphate buffer (pH 6.8) containing 0.03% NaN_3 and a set of protease inhibitors.

Experimental NMR Details. Figure 1 shows the two-dimensional (2D) *intra*-HN[CA/CO] pulse-scheme that has been designed for precision measurements of deuterium isotope effects on the chemical shifts of backbone ^{15}N, ^{1}HN, ^{13}CO, and $^{13}C^{\alpha}$ nuclei of proteins. The isotope effects on ^{15}N and ^{1}HN nuclei are quantified from the differences in chemical shifts of cross-peaks obtained at the frequencies ($\omega_{HN,I}$; ω_{Ni}) of 2D [^{1}HN,^{15}N] correlation maps (insets ***A***-***B*** omitted), while those on $^{13}CO_{i-1}$ and $^{13}C_{\alpha,i}$, nuclei are obtained from the differences in peak positions of 2D [^{1}HN,$^{13}CO_{i-1}$] and [^{1}HN,$^{13}C_{\alpha,i}$] maps (inset ***A*** or ***B*** included) at the corresponding frequencies ($\omega_{HN,i}$; $\omega_{CO,i-1}$) and ($\omega_{HN,i}$; $\omega_{C\alpha,i}$). 2D data sets are recorded with various combinations of filtering schemes via inclusion or omission of filtering elements F_1-F_3 resulting in individual subspectra that isolate the molecular species with each of the deuteration patterns shown in Figure 2 (see below and the 'Results and Discussion' section).

All narrow(wide) rectangular pulses in Figure 1 are applied with the flip angles of 90°(180°) along the *x*-axis unless indicated otherwise. The ^{1}H(^{2}H;^{15}N) carriers are positioned at 4.7(4.0;119) ppm. The ^{13}C carrier is placed at 57 ppm, switched to 176 ppm before the first 90° ^{13}CO pulse (after the gradient g5), returned to 57 ppm after the gradient g6, then placed back at 176 ppm after the gradient g8, and returned to 57 ppm before the ^{15}N pulse with phase ϕ4. If inset ***A*** is included for recording of [^{1}HN,$^{13}CO_{i-1}$] maps, the ^{13}C carrier is shifted to 176 ppm before inset ***A***. ^{15}N WALTZ-16[44] decoupling during acquisition is achieved using a 1.25 kHz field, while ^{2}H WALTZ-16 decoupling uses a 0.9 kHz field. ^{1}H DIPSI-2[45] decoupling is applied with a 7.5 kHz field. All ^{1}H and ^{15}N pulses are applied with maximum possible power, while the ^{1}H pulse shown with an arc (preceding the gradient g3) is implemented as a water-selective 1.4-ms pulse of rectangular shape. All rectangular 90°(180°) $^{13}C_\alpha$ and ^{13}CO pulses are applied with a field strength of $\Delta/\sqrt{15}(\Delta/\sqrt{3})$ where Δ is the difference (in Hz) between $^{13}C_\alpha$ and ^{13}CO chemical shifts.[46] Vertical arrows at the end of $2\tau_c$ periods and in the insets ***A***-***B*** indicate the positions of the $^{13}C_\alpha/^{13}$CO Bloch-Siegert shift compensation pulses.[46] $^{13}C_\beta$ shaped pulses in the middle of $2\tau_d$ periods are 1.52-ms I-BURP2[47] pulses centered at 30 ppm by phase modulation of the carrier[48,49] (inversion bandwidth of 17 ppm at 600 MHz). $^{13}C_\alpha$ shaped pulses labeled with 'α' in the middle of T_D and $T_D/2$ periods (insets F_3) are on-resonance 1.55-ms I-BURP2 pulses that cover the range of $^{13}C_\alpha$ resonances of all residues except Gly. ^{13}C shaped pulses in insets F_3 and ***B*** labeled with asterisks are 340-μs RE-BURP[47] pulses centered at 40 ppm by phase modulation of the carrier and cover the range of all aliphatic ^{13}C chemical shifts. Open pulses in insets F_3 are centered at 30 ppm (the center of $^{13}C_\beta$ region) by phase modulation of the carrier. Delays are as follows: τ_a = 2.7 ms; τ_b = 25 ms; τ_c = 4.5 ms; τ_d = 1.75 ms; T_N = 16.3 ms; T_C = 7.0 ms; T_D = 3.5 ms; δ = 5.4 ms; Δ = 400 μs. Delay ε (inset ***A***) is equal to the length of the 180° ^{15}N pulse. The phase-cycle used for acquisition of 2D [^{1}HN-^{15}N] maps (insets ***A***, ***B***, and F_3 omitted): $\phi1 = 4(x),4(-x)$; $\phi2 = x,-x$; $\phi3 = 8(x),8(-x)$; $\phi4 = 2(x),2(-x)$; $\phi5 = 16(x),16(-x)$; $\phi6 = x$; rec. = *x*,-*x*,-*x*,*x*, *x*,-*x*,-*x*,*x*, -*x*,*x*,*x*,-*x*, -*x*,*x*,*x*,-*x* for selection of $H_{\alpha,i-1}H_{\alpha,i}$ species (Figure 2a), rec. = *x*,-*x*,-*x*,*x*, -*x*,*x*,*x*,-*x*, *x*,-*x*,-*x*,*x*, -*x*,*x*,*x*,-*x* for $H_{\alpha,i-1}D_{\alpha,i}$ selection (Figure 2b), rec. = *x*,-*x*,-*x*,*x*, -*x*,*x*,*x*,-*x*, -*x*,*x*,*x*,-*x*, *x*,-*x*,-*x*,*x* for $D_{\alpha,i-1}H_{\alpha,i}$ selection (Figure 2c), and rec. = *x*,-*x*,-*x*,*x*, *x*,-*x*,-*x*,*x*, *x*,-*x*,-*x*,*x*, *x*,-*x*,-*x*,*x* for $D_{\alpha,i-1}D_{\alpha,i}$ selection (Figure 2d). 2D [^{1}HN-^{15}N] spectra with filtering elements F_3 included for selection of $^{13}C_\beta$HD and $^{13}C_\beta D_2$ molecular species (Figure 2e-f) are acquired with omission of the F_1 element, $\phi7 = 4(x),4(-x)$ in the $^{13}C_\beta$HD selection, and the rest of the phase cycle as above. The phase-cycle used for acquisition of [^{1}HN-$^{13}CO_{i-1}$] and [^{1}HN-$^{13}C_{\alpha,i}$] maps (insets ***A***, ***B***; inset F_3 omitted) are acquired with $\phi4 = x$; $\phi8 = \phi9 = 2(x),2(-x)$, and the rest of the phase-cycle as above. Inset ***D*** shows the part of the scheme enclosed in ***C*** used for longer acquisition times ($t_1 > 2\tau_b$). Quadrature detection in t_1 of the [^{1}HN-^{15}N] maps is achieved via the Rance-Kay scheme: for each t_1 value a pair of spectra is recorded with ($\phi6 = x$; g10) and ($\phi6 = -x$; -g10) and manipulated postacquisition.[50,51] The phase $\phi4$ is inverted for each t_1 point.[52] Quadrature detection in t_1 of the [^{1}HN-^{13}CO] and [^{1}HN-$^{13}C_\alpha$] spectra (insets ***A*** and ***B***) is achieved via STATES-TPPI[52] of phases $\phi8$ and $\phi9$, respectively. Durations and strengths of pulsed-field gradients in units of (ms; G/cm) are as follows: g1 = (1; 18); g2 = (0.25; 5); g3 = (1.2; 15); g4 = (1.0; 12); g5 = (0.6; 10); g6 = (0.8; 8); g7 = (0.7; 15); g7′ = (0.7; 12); g8 = (0.6; 8); g9 = (0.5; 12); g10 = (1.25; 20); g11 = (0.3; 15); g12 = (0.4; 12); g13 = (0.0625; 20); g14 = (0.0625; −20).

NMR Measurements and Data Analysis. All NMR measurements were performed on a 600 MHz Bruker Avance III spectrometer equipped with a room temperature triple-resonance *z*-gradient probe operating at 27 °C. 2D NMR data sets recorded with the pulse scheme of Figure 1, comprised [512, 82] complex points in the corresponding dimensions of the [^{1}HN,^{15}N] maps, [512, 42] complex points in the corresponding dimensions of the [^{1}HN,$^{13}C_{\alpha,i}$] maps, and [512, 128] complex points in the corresponding dimensions of the [^{1}HN,$^{13}CO_{i-1}$] maps, with the respective acquisition times of [64 ms, 49 ms], [64 ms, 28 ms] and [64 ms, 85 ms]. Typically, a recovery delay of 1.5 s was used along with 32 or 64 scans/FID giving rise to net acquisition times between 2.5 and 4.0 h./experiment. The [HN-^{15}N] and [HN-$^{13}C_{\alpha,i}$] data sets have been mirror-image linear-predicted[53] in the indirect dimension to twice their original sizes. ^{1}HN isotope shifts have been derived from 2D [^{1}HN,^{15}N] correlation maps acquired with twice the number of points in the acquisition dimension (1024*; $t_{2,max}$ = 108 ms) with otherwise the same set of acquisition parameters.

dx.doi.org/10.1021/jp304300n | J. Phys. Chem. B 2012, 116, 7436−7448

All NMR spectra were processed using the NMRPipe/NMRDraw suite of programs[54] and analyzed using either NMRDraw[54] or PIPP[55] software. As many of the measured displacements in peak positions resulting from deuterium isotope effects are small in magnitude (below the line-widths of resonances at half-height and the nominal digital resolution of the 2D data sets), we verified that the derived isotope shift values are reproducible using two different algorithms for determination of peak positions: (1) parabolic interpolation of intensities in both dimensions[54] and (2) fitting of 2D peak contours to elliptical shapes.[55] Highly correlated values ($R > 0.995$) have been obtained with both methods for well-separated correlations. All ^{15}N isotope shifts derived from the linear-predicted [HN-^{15}N] spectra have been compared with those derived from the 2D maps acquired with twice the number of points in t_1 using inset ***D*** of the scheme in Figure 1 for $t_1 > 2\tau_b$. In all the cases, and irrespective of the algorithm used for extraction of peak positions, the measured isotope shifts values were highly reproducible ($R > 0.99$) for sets of separated peaks. Each of the isotope shift measurements has been performed at least twice, and random uncertainties in the measurements estimated from pairwise rmsd between duplicate experiments. Since the accuracy of determination of peak positions increases with the signal-to-noise ratio,[56,57] several weak correlations (typically, Leu,[8] Leu,[15] Thr,[12] and Ala[46]) were not reproducible between different sets of data and excluded from analysis of some of the isotope effects.

One-bond C_α-H_α scalar couplings ($^1J_{C\alpha\text{-}H\alpha}$) have been measured on [U-^{15}N; ^{13}C]-labeled ubiquitin dissolved in 99.9% D_2O using (i) the quantitative-*J* approach of Tjandra and Bax[58] and (ii) from the splittings in the t_1-undecoupled $^1H_\alpha$-$^{13}C_\alpha$ correlation maps. An excellent agreement was obtained between the sets of $^1J_{C\alpha\text{-}H\alpha}$ values obtained using the two methods (pairwise rmsd of 0.5 Hz) as well as with $^1J_{C\alpha\text{-}H\alpha}$ couplings reported earlier.[58] $^1J_{C\alpha\text{-}H\alpha}$ couplings in ubiquitin vary between 134 and 151 Hz, and an average value of 143 Hz has been used for the calculation of the delays τ_d in the filter elements $\boldsymbol{F_1}$ and $\boldsymbol{F_2}$ of Figure 1.

Deuterium isotope effects on the chemical shifts of backbone nucleus *X* resulting from the substitution of a proton nucleus for deuterium at α site i ($^1H_{\alpha,i} \rightarrow D_{\alpha,i}$) are defined as $^n\Delta X(C_{\alpha,i}D) = \delta X(H_{\alpha,i}) - \delta X(D_{\alpha,i})$, where *n* is the number of bonds between the observed nucleus *X* and the position of the isotopic H→D substitution.[18,27] Best fits between the observed isotope shifts and backbone torsion angles were calculated via the least-squares minimization using Matlab (MathWorks Inc., MA). Dihedral angles (φ; ψ) used for the derivation of empirical relationships have been obtained from the 1.8 Å crystal structure of ubiquitin (pdb code −1ubq).[43] However, none of the conclusions of this study change significantly when the dihedral angles from the X-ray structure of chemically synthesized ubiquitin (pdb code -1ubi)[59,60] or the average angles from the ensemble of 10 NMR structures (pdb code -1d3z)[61] are used. The pairwise rmsd between the (φ; ψ) sets of angles of all these structures is on the order of 4-to-5° - too small a difference to significantly affect the treatment of isotope shifts in terms of backbone geometry.

RESULTS AND DISCUSSION

Experimental NMR Strategy for Accurate Measurements of Deuterium Isotope Shifts of Backbone Nuclei Resulting from $^1H_\alpha \rightarrow D_\alpha$ Substitutions. Two-dimensional [^{1}HN-^{15}N] versions of conventional triple-resonance experiments, such as HN(COCA)[62,63] and HN(CA),[46,63] do not provide high-resolution correlation maps of satisfactory quality in a partially deuterated protein even if the selection for either $C_\alpha H_\alpha$ or $C_\alpha D_\alpha$ spin-pairs is employed (e.g., using the single filtering element $\boldsymbol{F_2}$ of Figure 1). For example, because of the same isotope effects whose measurement is sought here, a high-resolution 2D [^{1}HN-^{15}N] correlation map of an HN(COCA) experiment (which transfers the magnetization through the ^{13}CO and $^{13}C_\alpha$ spins of the preceding residue, i-1) performed with selection for either $C_{\alpha,i\text{-}1}H_{\alpha,i\text{-}1}$ or $C_{\alpha,i\text{-}1}D_{\alpha,i\text{-}1}$ spin-pairs features two cross-peaks with ^{1}HN/^{15}N chemical shifts corresponding to $C_{\alpha,i}H_{\alpha,i}$ and $C_{\alpha,i}D_{\alpha,i}$ spin-pairs of residue i. Similarly, a high-resolution 2D [^{1}HN-^{15}N] correlation map of the HN(CA) experiment shows the following: (i) the same two peaks as above for the inter-residual (i-1) component of the signal and (ii) a (partially resolved) doublet for the intraresidual component of the signal due to isotope shifts resulting from the presence of $C_{\alpha,i\text{-}1}H_{\alpha,i\text{-}1}$ and $C_{\alpha,i\text{-}1}D_{\alpha,i\text{-}1}$ spin-pairs in the preceding residue. A 2D [^{1}HN-^{15}N] correlation map of the *intra*-HN(CA) experiment,[64−66] which transfers the magnetization through intraresidual $^{13}C_{\alpha,i}$ spins only, would show the same (partially resolved) doublets due to the isotope shifts arising from the presence of $C_{\alpha,i\text{-}1}H_{\alpha,i\text{-}1}$ and $C_{\alpha,i\text{-}1}D_{\alpha,i\text{-}1}$ spin-pairs in the preceding residue. Clearly, the measurement of changes in peak positions from such spectra is not reliable.

The *intra*-HN[CA/CO] pulse-scheme in Figure 1 employs two BIRD-type[67,68] filtering elements in succession ($\boldsymbol{F_1}$ and $\boldsymbol{F_2}$) to obtain correlations corresponding to only one type of molecular species with a defined protonation/deuteration pattern at two successive carbon-α sites. The schemes of dipeptide fragments with various patterns of protonation/deuteration at aliphatic (α/β) positions are shown in Figure 2. Double-filtering achieved by the elements $\boldsymbol{F_1}$ and $\boldsymbol{F_2}$ of the scheme (Figure 1) ensures isolation of NMR signals corresponding to each type of molecular species: $H_{\alpha,i\text{-}1}H_{\alpha,i}$ (2a), $H_{\alpha,i\text{-}1}D_{\alpha,i}$ (2b), $D_{\alpha,i\text{-}1}H_{\alpha,i}$ (2c), and $D_{\alpha,i\text{-}1}D_{\alpha,i}$ (2d). This is accomplished in the following manner. At time point *a* of the *intra*-HN(CA) scheme in Figure 1, the magnetization of interest is present in the form, $8N_{z,i}CO_{z,i\text{-}1}C^\alpha{}_{y,i\text{-}1}C^\alpha{}_{y,i}{}^{64}$ (here and below we omit the trigonometric factors and all the terms that do not lead to observable magnetization in the end of the scheme). The molecular species having different isotopic content can be differentiated based on evolution of $^1J_{C\alpha\text{-}H\alpha}$ couplings in $C_\alpha H_\alpha$ spin-systems for a total period of $4\tau_d = 1/^1J_{C\alpha\text{-}H\alpha}$ (Figure 1) and the lack thereof in $C_\alpha D_\alpha$ groups - in a manner very similar to the filtering schemes proposed earlier by Meissner and Sørensen for isotope shift measurements in proteins.[28,29] In the presence of $^1J_{C\alpha\text{-}H\alpha}$ evolution ($\phi 1 = x$), after the time-period $4\tau_d$ in the first element $\boldsymbol{F_1}$ (time point *b* of the scheme), the magnetization transforms as follows

$$8N_{z,i}CO_{z,i-1}C^\alpha{}_{y,i-1}C^\alpha{}_{y,i} \rightarrow \pm 8N_{z,i}CO_{z,i-1}C^\alpha{}_{y,i-1}C^\alpha{}_{y,i} \quad (1)$$

where the $H_{\alpha,i\text{-}1}H_{\alpha,i}$ and $D_{\alpha,i\text{-}1}D_{\alpha,i}$ molecular species retain their sign ('+'), while their $H_{\alpha,i\text{-}1}D_{\alpha,i}$ and $D_{\alpha,i\text{-}1}H_{\alpha,i}$ counterparts will be inverted ('-'). The concomitant cycling of the phase $\phi 1$ and the receiver phase selects for either pair of molecular species. Subsequently, the magnetization is transformed to $4N_{z,i}CO_{z,i\text{-}1}C^\alpha{}_{y,i}$ at time-point *c* of the scheme (Figure 1). In the presence of $^1J_{C\alpha\text{-}H\alpha}$ evolution ($\phi 3 = x$), after the $4\tau_d$ time-period (time point *d* in the second element $\boldsymbol{F_2}$; Figure 1) this magnetization transforms as

dx.doi.org/10.1021/jp304300n | J. Phys. Chem. B 2012, 116, 7436−7448

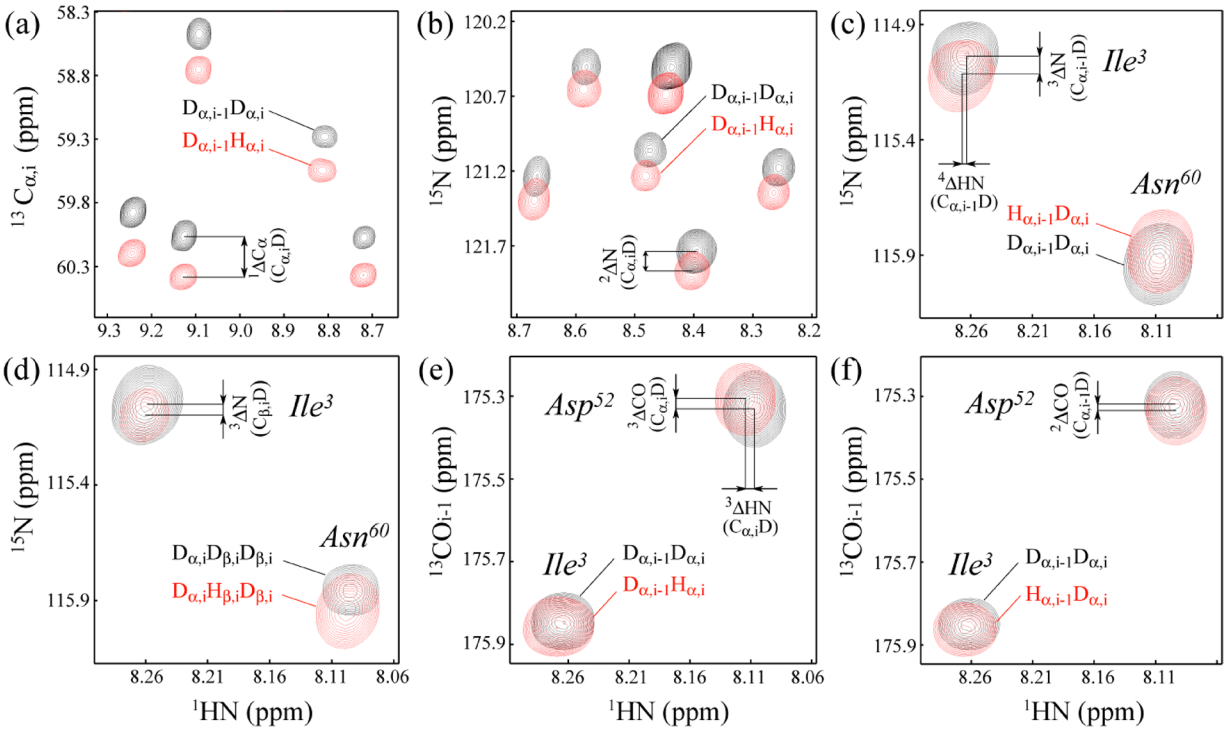

Figure 3. Superposition of selected regions of high-resolution 2D *intra*-HN[CA/CO] correlation maps showing the displacement of peak positions resulting from $^{1}H\rightarrow D$ substitutions at α or β sites. Cross-peaks shown with red (black) contours correspond to the protonated (deuterated) molecular species as indicated on the plots using the notation defined in Figure 2: **(a)** [HN-$^{13}C_{\alpha,i}$] correlation map for the measurement of $^{1}\Delta C_{\alpha}(C_{\alpha,i}D)$ isotope shifts; **(b)** [HN-^{15}N] correlation map for the measurement of $^{2}\Delta N(C_{\alpha,i}D)$ shifts; **(c)** [HN-^{15}N] correlation map for the measurement of $^{3}\Delta N(C_{\alpha,i-1}D)$ shifts; **(d)** [HN-^{15}N] correlation map for the measurement of $^{3}\Delta N(C_{\beta,i}D)$ shifts. Peak displacements in the HN dimension of the spectra shown in (c) and (e) allow the measurements of $^{4}\Delta HN(C_{\alpha,i-1}D)$ and $^{3}\Delta HN(C_{\alpha,i}D)$ effects; **(e)** [HN-$^{13}CO_{i-1}$] correlation map for the measurement of $^{3}\Delta CO(C_{\alpha,i}D)$ isotope shifts; **(f)** [HN-$^{13}CO_{i-1}$] correlation map for the measurement of $^{2}\Delta CO(C_{\alpha,i-1}D)$ shifts.

$$4N_{z,i}CO_{z,i-1}C^{\alpha}_{y,i} \rightarrow \pm 4N_{z,i}CO_{z,i-1}C^{\alpha}_{y,i} \qquad (2)$$

where the species of $H_{\alpha,i-1}D_{\alpha,i}$ and $D_{\alpha,i-1}D_{\alpha,i}$ variety will retain their sign ('+'), while their $D_{\alpha,i-1}H_{\alpha,i}$ and $H_{\alpha,i-1}H_{\alpha,i}$ counterparts will be inverted ('-'). Note that the filtering at the second stage (2) acts only on $C_{\alpha,i}H_{\alpha,i}/C_{\alpha,i}D_{\alpha,i}$ spin-pairs of residue i. The cycling of the phase $\phi 3$ and the receiver phase selects only a single type of molecular species from each pair of species that had been previously selected by the element $\boldsymbol{F}_1$ (1). Thus, isolation of NMR signals of each type of species in Figure 2a-d results in four separate subspectra, while the isotope shifts due to $^{1}H\rightarrow D$ substitutions at C_{β} positions remain unresolved. The 'double-filtering' strategy described above achieves separation of two- and three-bond as well as three- and four-bond deuterium isotope effects that can be comparable in magnitude and (at least in some of the cases analyzed below) cannot be left unresolved because they would otherwise lead to broadening of resonances or appearance of doublet cross-peak structures.

Additional filtering elements $\boldsymbol{F}_3$ (Figure 1) can be used to separate the molecular species with either CHD or CD_2 groups at β sites. Two types of $\boldsymbol{F}_3$ filtering are used resulting in isolation of molecular species of $D_{\alpha,i}H_{\beta,i}D_{\beta,i}$ (Figure 2e) and $D_{\alpha,i}D_{\beta,i}D_{\beta,i}$ (Figure 2f) variety for the measurements of isotope effects of the $^{1}H^{\beta}\rightarrow D^{\beta}$ substitution on ^{15}N chemical shifts. Here, the $C_{\beta}HD$ spin-systems are isolated in the same manner as described above for the spin-systems at α positions (inset $\boldsymbol{F}_3(^{13}C_{\beta}HD)$; Figure1), while the $C_{\beta}D_2$ groups are distinguished from their $C_{\beta}H_2$ and $C_{\beta}HD$ counterparts via the evolution of $^{1}J_{C\beta\text{-}H\beta}$ couplings (~140 Hz) for a total period of $T_D = 1/(2^{1}J_{C\beta\text{-}H\beta})$ in the latter spin-systems (inset $\boldsymbol{F}_3(^{13}C_{\beta}D_2)$; Figure 1). In the spin-systems with at least one proton ($C_{\beta}H_2$ and $C_{\beta}HD$), such evolution leads to creation of magnetization terms that include H^{β}_{z} operator(s), which are not refocused with respect to protons in the end of the experiment. In principle, the filtering elements $\boldsymbol{F}_3$ can be used together with $\boldsymbol{F}_1$ and $\boldsymbol{F}_2$. In practice, however, sensitivity of such 2D spectra is severely compromised; it is therefore preferable to leave the three-bond ^{15}N shifts, $^{3}\Delta N(C_{\alpha,i-1}D)$, unresolved by omitting the element $\boldsymbol{F}_1$ in $^{3}\Delta N(C_{\beta,i}D)$ measurements.

Examples of displacements of peak positions in high-resolution 2D *intra*-HN[CA/CO] correlation maps arising from the isotope effects of the $^{1}H\rightarrow D$ substitutions at α_i or α_{i-1} positions and β_i sites are illustrated in Figure 3: (i) $^{1}\Delta C_{\alpha}(C_{\alpha,i}D)$ isotope shifts are measured from the [HN-$^{13}C_{\alpha,i}$] correlation maps (3a), (ii) $^{2}\Delta N(C_{\alpha,i}D)$, $^{3}\Delta N(C_{\alpha,i-1}D)$, and $^{3}\Delta N(C_{\beta,i}D)$ shifts are measured from the [HN-^{15}N] correlation maps (3b,c and d), while (iii) $^{3}\Delta CO(C_{\alpha,i}D)$ and $^{2}\Delta CO$-$(C_{\alpha,i-1}D)$ isotope effects are measured from the [HN-$^{13}CO_{i-1}$] maps (3e,f). The differences in chemical shifts between protonated and deuterated molecular species defined in Figure 2 are labeled with the corresponding isotope effect in each of the maps. The relation between average signal-to-noise ratios obtained in 2D [^{1}HN-^{15}N] correlation subspectra acquired with selection of the corresponding molecular species is $(D_{\alpha,i-1}D_{\alpha,i})$:$(H_{\alpha,i-1}D_{\alpha,i})$:$(D_{\alpha,i-1}H_{\alpha,i})$:$(H_{\alpha,i-1}H_{\alpha,i})$ = 1.0:0.60:0.55:0.36 - in agreement with the expected ratios of 1.0:0.67:0.67:0.44 based on 40% protonation of the sample, assuming random protonation at two neighboring α sites and neglecting faster ^{13}C relaxation in C_{α}-H_{α} spin-pairs.

dx.doi.org/10.1021/jp304300n | J. Phys. Chem. B 2012, 116, 7436−7448

Clearly, the selection of all molecular species listed in Figures 2a-d is not necessary for the measurement of each given isotope shift. However, because many of the measured effects are small in magnitude, we feel it is imperative to ascertain the consistency of the shifts derived from different combinations of subspectra. Figure S1 (Supporting Information) shows the correlation plots illustrating the agreement between (a) $^2\Delta N(C_{\alpha,i}D)$ shifts measured from the ($H_{\alpha,i\text{-}1}H_{\alpha,i}$ vs $H_{\alpha,i\text{-}1}D_{\alpha,i}$) combination of subspectra and the same shifts derived from the ($D_{\alpha,i\text{-}1}H_{\alpha,i}$ vs $D_{\alpha,i\text{-}1}D_{\alpha,i}$) combination; (b) $^3\Delta N(C_{\alpha,i\text{-}1}D)$ shifts measured from the ($H_{\alpha,i\text{-}1}H_{\alpha,i}$ vs $D_{\alpha,i\text{-}1}H_{\alpha,i}$) combination of subspectra and the same shifts derived from the ($H_{\alpha,i\text{-}1}D_{\alpha,i}$ vs $D_{\alpha,i\text{-}1}D_{\alpha,i}$) combination, and (c) $^3\Delta CO(C_{\alpha,i}D)$ shifts measured from the ($H_{\alpha,i\text{-}1}H_{\alpha,i}$ vs $H_{\alpha,i\text{-}1}D_{\alpha,i}$) combination and the same shifts derived from the ($D_{\alpha,i\text{-}1}H_{\alpha,i}$ vs $D_{\alpha,i\text{-}1}D_{\alpha,i}$) combination. Although all the data sets are highly correlated ($R > 0.98$), for sensitivity reasons (see above), we prefer to use the combinations of more deuterated species for derivation of isotope shifts, e.g. ($H_{\alpha,i\text{-}1}D_{\alpha,i}$ vs $D_{\alpha,i\text{-}1}D_{\alpha,i}$) subspectra instead of ($H_{\alpha,i\text{-}1}H_{\alpha,i}$ vs $D_{\alpha,i\text{-}1}H_{\alpha,i}$) subspectra for $^3\Delta N(C_{\alpha,i\text{-}1}D)$ measurements and ($D_{\alpha,i\text{-}1}H_{\alpha,i}$ vs $D_{\alpha,i\text{-}1}D_{\alpha,i}$) subspectra instead of ($H_{\alpha,i\text{-}1}H_{\alpha,i}$ vs $H_{\alpha,i\text{-}1}D_{\alpha,i}$) for $^2\Delta N(C_{\alpha,i}D)$ measurements.

It is important to realize that two- and three-bond as well as three- and four-bond isotope shifts can be comparable in magnitude. The approach adopted here cleanly separates the changes in chemical shifts due to each distinct isotope effect. For example, taking the difference between chemical shifts in the ($D_{\alpha,i\text{-}1}H_{\alpha,i}$; $D_{\alpha,i\text{-}1}D_{\alpha,i}$) pairs of data sets for $^2\Delta N(C_{\alpha,i}D)$ measurements (Figure 3b) and the ($H_{\alpha,i\text{-}1}D_{\alpha,i}$; $D_{\alpha,i\text{-}1}D_{\alpha,i}$) pairs of subspectra for $^3\Delta N(C_{\alpha,i\text{-}1}D)$ measurements (Figure 3c) ensures separation of these two isotope effects on ^{15}N nuclei. Nevertheless, in glycine residues, the filtering elements $\boldsymbol{F}_1$ and $\boldsymbol{F}_2$ (Figure 1) cannot differentiate between fully protonated (CH_2) and fully deuterated (CD_2) α sites. This leads to compromised values of isotope shifts in the residues following glycine and (in some cases, when the chemical shifts corresponding to CH_2 and CD_2 α_i-sites are not well resolved) compromised isotope shift values of glycines themselves. Therefore, isotope shifts measured in the residues preceded by Gly and in Gly itself should be interpreted with caution and are excluded from analysis of some of the isotope effects in terms of backbone geometry. Even though the elements $\boldsymbol{F}_3$ can distinguish between Gly $C_\alpha H_2$ and $C_\alpha D_2$ spin-systems, their use instead of $\boldsymbol{F}_1$ and/or $\boldsymbol{F}_2$ leads to significant decrease in the sensitivity of the experiments and has not been pursued here.

In what follows we describe the isotope effects on the backbone nuclei resulting from $^1H\rightarrow D$ substitutions at aliphatic carbon positions (primarily α sites) in the order of their decreasing magnitude and delineate their quantitative dependence on the backbone geometry of ubiquitin.

One-Bond Carbon-α Isotope Shifts, $^1\Delta C_\alpha(C_{\alpha,i}D)$. The substitution of a directly attached proton nucleus for a deuteron at carbon-α sites results in relatively large changes of $^{13}C_\alpha$ chemical shifts. Usually, however, the values of one-bond $^{13}C_\alpha$ shifts, $^1\Delta C_\alpha(C_{\alpha,i}D)$, are estimated from comparisons of $^{13}C_\alpha$ chemical shifts between fully deuterated and fully protonated protein molecules,[1,14,35,69] leading to some overestimation of the one-bond isotope shifts due to the combined effects of one-, two-, and three-bond $^1H\rightarrow D$ substitutions (isotope effects of deuteration at C_β, C_γ *etc.* sites). The approach adopted here is more robust because partial deuteration of the protein molecule results in unresolved two- and three-bond isotope effects, leaving the [HN-$^{13}C_{\alpha,i}$] cross-peak displacements shown in Figure 3a, largely unaffected by higher order shifts. The average $^1\Delta C_\alpha(C_{\alpha,i}D)$ value of 314 ± 35 ppb has been measured in ubiquitin from the displacements of cross-peaks between the $D_{\alpha,i\text{-}1}H_{\alpha,i}$ and $D_{\alpha,i\text{-}1}D_{\alpha,i}$ subspectra (Figure 2c,d and Figure 3a). The plot of $^1\Delta C_\alpha(C_{\alpha,i}D)$ shifts versus the sequence of ubiquitin is shown in Figure S2a of the Supporting Information. A weak dependence of $^1\Delta C_\alpha(C_{\alpha,i}D)$ on the protein secondary structure has been noted earlier by several investigators.[14,35,39,40,69] Indeed, the $^1\Delta C_\alpha(C_{\alpha,i}D)$ values in the α-helical region of ubiquitin are higher than in the β-structures and loops (Figure S2a; the largest $^1\Delta C_\alpha(C_{\alpha,i}D)$ values are 428 and 415 ppb for Val[26] and Ile[30] in the α-helix of ubiquitin, respectively).

Similarities between the dependence of $^1\Delta C_\alpha(C_{\alpha,i}D)$ and one-bond scalar couplings, $^1J_{C\alpha\text{-}H\alpha}$, on backbone dihedral angles, have been noted previously for glycine residues by LeMaster and co-workers.[39] $^1J_{C\alpha\text{-}H\alpha}$ couplings measured in ubiquitin are plotted versus the sequence in Figure S2b (Supporting Information). The dependence of $^1J_{C\alpha\text{-}H\alpha}$ (Hz) on dihedral angles (ϕ; ψ) is best described by the relationship

$$^1J_{C\alpha-H\alpha}\ (\mathrm{Hz}) = 141.5 + 1.7\sin(\psi + 139^\circ) - 4.7\cos[2(\psi + 139^\circ)] + 1.8\cos[2(\phi + 20^\circ)] \quad (3)$$

which is very similar to the $^1J_{C\alpha\text{-}H\alpha}$ vs (ϕ; ψ) dependence reported earlier,[58,70] with the pairwise rmsd between the measured and back-calculated $^1J_{C\alpha\text{-}H\alpha}$ couplings of only 1.5 Hz (Figure S3a; Supporting Information). The measured $^1\Delta C_\alpha(C_{\alpha,i}D)$ isotope shifts (in ppb) are best-fit to a similar function of (ϕ; ψ) angles

$$^1\Delta C_\alpha(C_{\alpha,i}D) = 342.5 + 34.1\sin(\psi + 187^\circ) - 40.3\cos[2(\psi + 187^\circ)] + 19.9\cos[2(\phi + 42^\circ)] \quad (4)$$

As shown in Figures S3b-c the agreement between the measured and predicted $^1\Delta C_\alpha(C_{\alpha,i}D)$ shifts is significantly worse than in the case of $^1J_{C\alpha\text{-}H\alpha}$ couplings (pairwise rmsd between measured and back-calculated values of 25 ppb), with the largest discrepancies observed for helical residues Val,[26] Ile,[30] Asp,[32] Asp,[58] and Asp[52] in the bend (Figure S3b). Even upon elimination of these residues from the fit, the pairwise rmsd between experimental and calculated values remains high in comparison to the range of measured $^1\Delta C_\alpha(C_{\alpha,i}D)$ shifts, ~100 ppb (Figure S3c; rmsd = 19 ppb, $R = 0.772$), while the coefficients in eq 4 change only slightly. Of note, the average measured $^1\Delta C_\alpha(C_{\alpha,i}D)$ (0.31 ppm) is very similar to one-bond isotope shifts in methyl groups arising from a single $^1H\rightarrow D$ substitution ($CH_3\rightarrow CH_2D$ or $CH_2D\rightarrow CHD_2$),[71] although it may be somewhat skewed toward lower values because of a limited number of residues in a helical conformation in ubiquitin.

The approach used in this work allows quantification of four-bond $^{13}C_\alpha$ isotope shifts resulting from $^1H\rightarrow D$ substitutions at $C_{\alpha,i\text{-}1}$ positions, $^4\Delta C_\alpha(C_{\alpha,i\text{-}1}D)$, from the comparison of chemical shifts in the $H_{\alpha,i\text{-}1}D_{\alpha,i}$ and $D_{\alpha,i\text{-}1}D_{\alpha,i}$ species (Figure 2b,d). The measured $^4\Delta C_\alpha(C_{\alpha,i\text{-}1}D)$ shifts are very small and positive (5 ± 4.8 ppb) and plotted versus the sequence of ubiquitin in Figure S4 (Supporting Information). Although some dependence on secondary structure can be noted from Figure S4, with the residues in β conformations having usually higher $^4\Delta C_\alpha(C_{\alpha,i\text{-}1}D)$ values than their counterparts in helical

dx.doi.org/10.1021/jp304300n | J. Phys. Chem. B 2012, 116, 7436−7448

regions, the small magnitude of these effects precludes their quantitative interpretation in terms of secondary structure.

Three- and Two-Bond Amide Nitrogen Isotope Shifts, $^3\Delta N(C_{\alpha,i\text{-}1}D)$, $^2\Delta N(C_{\alpha,i}D)$, and $^3\Delta N(C_{\beta,i}D)$. Three-bond ^{15}N isotope shifts resulting from $^1H\rightarrow D$ substitutions at $C_{\alpha,i\text{-}1}$ positions, $^3\Delta N(C_{\alpha,i\text{-}1}D)$, measured from the differences in chemical shifts of the $H_{\alpha,i\text{-}1}D_{\alpha,i}$ and $D_{\alpha,i\text{-}1}D_{\alpha,i}$ molecular species (Figure 2b,d; see examples of peak displacements in Figure 3c), are plotted versus the sequence of ubiquitin in Figure 4a, while

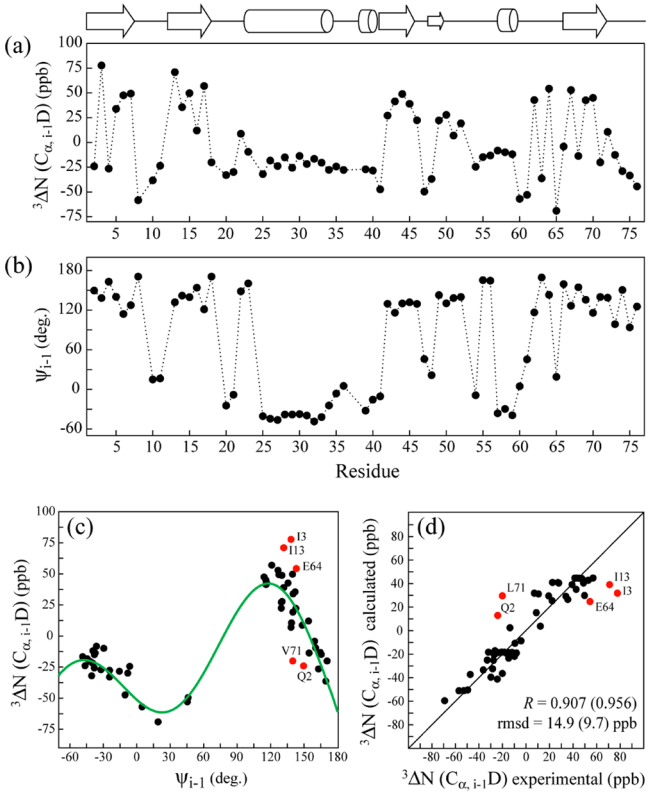

Figure 4. Plots of (**a**) the measured $^3\Delta N(C_{\alpha,i\text{-}1}D)$ shifts and (**b**) ψ dihedral angle of residue i-1 ($\psi_{i\text{-}1}$) versus the sequence of ubiquitin; (**c**) $^3\Delta N(C_{\alpha,i\text{-}1}D)$ isotope shifts plotted as a function of $\psi_{i\text{-}1}$ angles. The green curve represents the best-fit function, eq 5; (d) a correlation plot showing the agreement between experimental $^3\Delta N(C_{\alpha,i\text{-}1}D)$ values (*x*-axis) and the values predicted using eq 5 (*y*-axis) for 58 residues of ubiquitin. Residues shown with red circles and labeled show the worst agreement between the measured $^3\Delta N(C_{\alpha,i\text{-}1}D)$ shifts and those back-calculated using eq 5. Pearson correlation coefficient *R* and rmsd of the data in (d) are shown with and without (in parentheses) inclusion of residues marked in red. Schematic diagram of the secondary structure of ubiquitin is shown above panels (a-b) with arrows and cylinders denoting β-strands and helical regions, respectively.

Figure 4b shows ψ dihedral angles of residue i-1 ($\psi_{i\text{-}1}$) plotted versus the sequence of the protein. In the case of $^3\Delta N(C_{\alpha,i\text{-}1}D)$ isotope shifts, the angles $\psi_{i\text{-}1}$ represent dihedral angles formed by the three intervening bonds between the position of $^1H\rightarrow D$ substitution ($H_{\alpha,i\text{-}1}\rightarrow D_{\alpha,i\text{-}1}$) and the amide nitrogen ^{15}N of residue i (Figure 2b,d). Figure 4c shows $^3\Delta N(C_{\alpha,i\text{-}1}D)$ shifts plotted as a function of $\psi_{i\text{-}1}$ angles. The values of $^3\Delta N(C_{\alpha,i\text{-}1}D)$ shifts vary from −74 ppb (Ser^{65}) to +76 ppb (Ile^3). Clearly, higher $^3\Delta N(C_{\alpha,i\text{-}1}D)$ shifts usually correspond to β-strands (Figure 4a and 4c). Although some overlap between the $^3\Delta N(C_{\alpha,i\text{-}1}D)$ values in α- and β-structures exists, the $^3\Delta N(C_{\alpha,i\text{-}1}D)$ shifts in helices and β-turns are invariably *negative* and somewhat smaller in absolute magnitude.

The simplest trigonometric relationship that describes the dependence of $^3\Delta N(C_{\alpha,i\text{-}1}D)$ shifts on $\psi_{i\text{-}1}$ torsion angles is of the following form: $A + B\sin(\psi_{i\text{-}1}+C) + D\sin[2(\psi_{i\text{-}1}+C)]$. Upon exclusion of all ubiquitin residues disordered in solution (Leu^8-Thr^{12} and Leu^{73}-Gly^{76})[72] and the amide peaks of residues following glycines (*vide supra*), the least-squares best-fit yields

$$^3\Delta N(C_{\alpha,i-1}D)\ (\text{ppb}) = -39.4 + 45.3\sin(\psi_{i-1} + 8°) - 50.2\sin[2(\psi_{i-1} + 8°)] \quad (5)$$

with rmsd between the measured and back-calculated shifts of 14.9 ppb (Figure 4d; R = 0.907) - more than an order of magnitude lower than the range of $^3\Delta N(C_{\alpha,i\text{-}1}D)$ values (~150 ppb). Inclusion of additional parameters into the functional form in eq 5 that depend on either the ϕ angle of residue i (ϕ_i) or that of the previous residue ($\phi_{i\text{-}1}$) does not lead to statistically significant improvements in the fit as judging by *F*-statistics.[73] Five residues with the largest disagreement between experimental and predicted shifts are as follows: Gln,[2] Ile,[3] Ile,[13] Glu,[64] and Leu[71] (Figure 4c-d). Exclusion of these residues from the fit provides the relationship in eq 5 with A = −39.3, B = 43.8, C = 8°, and D = −49.0, with the rmsd between the measured and back-calculated values of 9.7 ppb (R = 0.956).

The amides of Ile,[3] Ile,[13] and Glu[64] are hydrogen-bonded in the structure of ubiquitin.[43] Even though it may be unreliable to estimate the strength of hydrogen bonds from the N−H···O=C distances in the 1.8 Å X-ray structure, strong hydrogen bonds are commonly associated with downfield amide proton isotropic chemical shifts, δ(HN).[27,74] Amide protons of Ile^{13} and Glu^{64} are two of the three most downfield-shifted amides in [^{1}HN-^{15}N] correlation maps of ubiquitin: δ(HN) = 9.52 and 9.25 ppm, respectively. In fact, statistically significant correlation is noted between the measured $^3\Delta N(C_{\alpha,i\text{-}1}D)$ shifts and δ(HN) for 65 amides of ubiquitin (Figure S5; Supporting Information), indicating that $^3\Delta N(C_{\alpha,i\text{-}1}D)$ shifts *increase* with the strength of hydrogen bonds. This is consistent with the behavior one would expect to observe for Ile,[3] Ile,[13] and Glu,[64] where experimental $^3\Delta N(C_{\alpha,i\text{-}1}D)$ shifts are larger than those predicted by eq 5 - likely owing to hydrogen bonding effects, whereas the amides of Gln[2] and Leu[71] are not hydrogen bonded and therefore have their measured $^3\Delta N(C_{\alpha,i\text{-}1}D)$ lower than predicted from eq 5 (Figure 4d). It is important to emphasize that in contrast to the effects of hydrogen bonding on the isotope shifts of backbone $^{13}C_\alpha$ and tyrosine $^{13}C_\zeta$ nuclei in proteins occurring upon the respective NH→ND and $O_\eta H$−$O_\eta D$ substitutions noted in earlier studies,[27,30] in the present work, hydrogen bonding possibly affects isotope shifts of the nuclei either attached to hydrogen bond donors/acceptors or directly involved in hydrogen bonding (backbone ^{15}N, ^{13}CO, ^1HN) rather than ^{13}C positions that 'feel' H→D substitutions at adjacent hydrogen bonds. Although based on the studies of small model compounds, two-bond ^{15}N shifts, such as $^2\Delta N(C_{\alpha,i}D)$ described below, are expected to be more prone to hydrogen bonding effects;[75] we speculate that hydrogen bonding that is predicted to increase the double-bond character of the peptide bond and thereby increase its planarity[76,77] might have a similar effect on $^3\Delta N(C_{\alpha,i\text{-}1}D)$ isotope shifts.

The dependence of $^3\Delta N(C_{\alpha,i\text{-}1}D)$ shifts on the dihedral angle $\psi_{i\text{-}1}$ is not surprising. The Karplus-type relationships between three-bond isotope shifts and the torsion angles formed by the

dx.doi.org/10.1021/jp304300n | J. Phys. Chem. B 2012, 116, 7436−7448

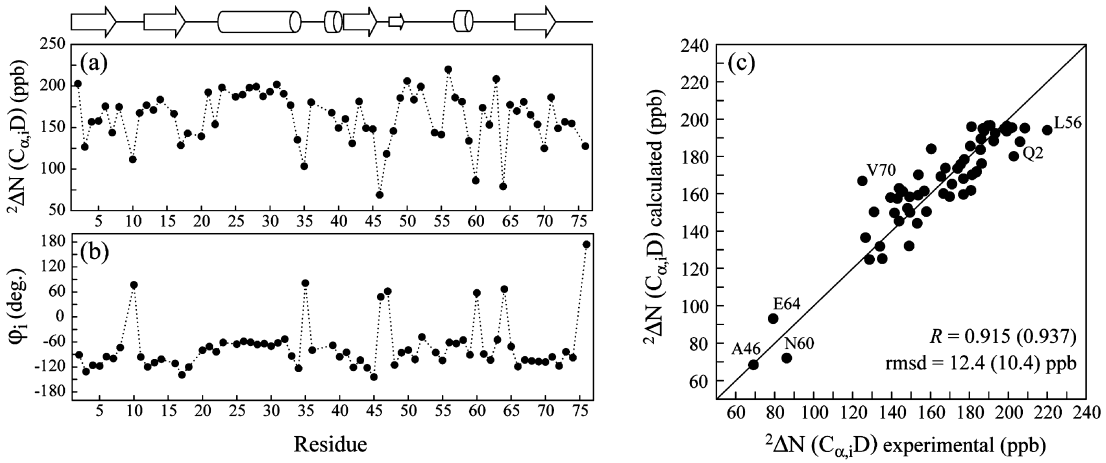

Figure 5. Plots of (**a**) $^2\Delta N(C_{\alpha,i}D)$ isotope shifts and (**b**) ϕ dihedral angles of residue i (ϕ_i versus the sequence of ubiquitin; (**c**) a correlation plot showing the agreement between experimental $^2\Delta N(C_{\alpha,i}D)$ shifts (*x*-axis) and those predicted from eq 6 (*y*-axis) for 59 residues of ubiquitin. Residues shown in red show the worst agreement with eq 6. Pearson correlation coefficient *R* and rmsd of the data in (c) are shown with and without (in parentheses) the residues marked in red. Nonglycine residues with *positive* ϕ angles (Ala,[46] Asn,[60] Glu[64]) are labeled with residue numbers. Schematic diagram of the secondary structure of ubiquitin is shown above panels (a-b), with arrows and cylinders denoting β-strands and helical regions, respectively.

intervening bonds have been noted in small model systems on multiple occasions previously.[18,20,41,42,78] The absence of such dependence in the earlier study by Ottiger and Bax,[27] that quantified three-bond $^3\Delta C_{\alpha,i-1}(ND)$ isotope effects resulting from NH→ND substitutions at amide positions, is related to the fact that in the latter case the relevant dihedral angle is the angle of the peptide bond (ω) which is almost invariable (ω = 180° to within ~5°,[77,79] even though a recent study contests this small range of ω variability[80]).

Two-bond ^{15}N isotope shifts resulting from $^1H\rightarrow D$ substitutions at $C_{\alpha,i}$ positions, $^2\Delta N(C_{\alpha,i}D)$, are measured from the differences in chemical shifts of the $D_{\alpha,i-1}H_{\alpha,i}$ and $D_{\alpha,i-1}D_{\alpha,i}$ molecular species (Figure 2c,d; see examples of peak displacements in Figure 3b) and plotted versus the sequence of ubiquitin in Figure 5a. A plot of dihedral angles ϕ of residue i (ϕ_i) versus the sequence of the protein is shown in Figure 5b. All the measured $^2\Delta N(C_{\alpha,i}D)$ shifts are positive and vary from 70 ppb (Ala[46]) to 220 ppb (Leu[56]). Although the dependence of $^2\Delta N(C_{\alpha,i}D)$ shifts on the secondary structure is not immediately obvious from Figure 5a (partly because of a limited variability of ϕ angles between different types of secondary structure), it can be noted that the smallest shifts correspond to the residues with *positive* ϕ angles: Ala,[46] Asn,[60] Glu,[64] Gly,[10] Gly,[35] and Gly[47] (Figure 5a-c). The simplest functional form that describes the dependence of $^2\Delta N(C_{\alpha,i}D)$ shifts on dihedral angles is as follows: $A + B\sin[2(\phi_i+C)] + D\sin(2\psi_i)$. Upon exclusion of all ubiquitin residues disordered in solution (Leu[8]-Lys[11] and Leu[73]-Gly[76])[72] and the shifts of Gly[35] and Gly[47] (*vide supra*), the least-squares best-fit yields the following relationship

$$^2\Delta N(C_{\alpha,i}D)\ (ppb) = 130.4 - 20.4\sin[2(\phi_i + 11°)] - 44.0\sin(2\psi_i) \quad (6)$$

with pairwise rmsd between the measured and back-calculated $^2\Delta N(C_{\alpha,i}D)$ values of 12.4 ppb (Figure 5c; $R = 0.915$) - more than 10 times lower than the variability range of $^2\Delta N(C_{\alpha,i}D)$ shifts (150 ppb if the residues with positive ϕ are considered). Inclusion of the angle ψ_i in the function of eq 6 leads to statistically significant improvements in the fit reducing the pairwise rmsd by 4 ppb. Three residues with the largest disagreements between experimental and predicted values are as follows: Gln,[2] Leu,[56] and Val[70] (Figure 5c). Exclusion of these residues practically does not change the parameters in eq 6 but significantly improves the fit providing the rmsd between measured and back-calculated $^2\Delta N(C_{\alpha,i}D)$ shifts of 10.4 ppb (Figure 5c; $R = 0.937$). The amides of Leu[56] and Val[70] are hydrogen bonded in the structure of ubiquitin. The amide proton of Val[70] is significantly downfield shifted - δ(HN) = 9.14 ppm - possibly indicating hydrogen bonding effects. The reasons for the larger than predicted $^2\Delta N(C_{\alpha,i}D)$ of Leu[56] located in a β-turn preceding the 3_{10}-helix Ser[57]-Tyr[59] and that of Gln[2] in the first β-strand are not clear at this point.

Three-bond ^{15}N isotope shift arising from the substitution of one of the β protons with a deuteron, $^3\Delta N(C_{\beta,i}D)$, have been quantified using the filtering elements $\boldsymbol{F}_2$ and $\boldsymbol{F}_3$ with the element $\boldsymbol{F}_1$ omitted from the scheme in Figure 1 for sensitivity reasons (leading to the isolation of molecular species shown in Figure 2e,f with the $^3\Delta N(C_{\alpha,i-1}D)$ isotope shifts remaining unresolved; see 'Materials and Methods' and examples of peak displacements in Figure 3d). The $^3\Delta N(C_{\beta,i}D)$ shifts are positive and vary from 12 to 82 ppb (mean $^3\Delta N(C_{\beta,i}D) = 46 \pm 15$ ppb) with a single exception of Ile[13] which reproducibly provided a negative $^3\Delta N(C_{\beta,i}D)$ shift of −7 ppb. A histogram plot of $^3\Delta N(C_{\beta,i}D)$ shifts is shown in Figure S6a (Supporting Information). The dihedral angle formed by the three intervening bonds in the case of $^3\Delta N(C_{\beta,i}D)$ isotope shifts is χ_1 (Figure 2e,f). However, no clear dependence of $^3\Delta N(C_{\beta,i}D)$ on χ_1 angles has been observed in ubiquitin - probably because of the averaging of side-chain rotameric states of many residues in solution and/or the likely dependence of $^3\Delta N(C_{\beta,i}D)$ shifts on the residue type. Even when the identified subset of ubiquitin residues for which no evidence of rotameric averaging exists from analysis of *J* couplings[79] is considered, quantitative correlations between $^3\Delta N(C_{\beta,i}D)$ shifts and χ_1 angles from the crystal structure remain elusive. This observation may be related to the fact that the filtering element $\boldsymbol{F}_3$ in the scheme of Figure 1 differentiates between $C_\beta D_2$ and $C_\beta HD$ groups where protonation can occur at any of the two pro-chiral β positions − i.e. the chirality of the H→D substitution is not controlled

dx.doi.org/10.1021/jp304300n | J. Phys. Chem. B 2012, 116, 7436−7448

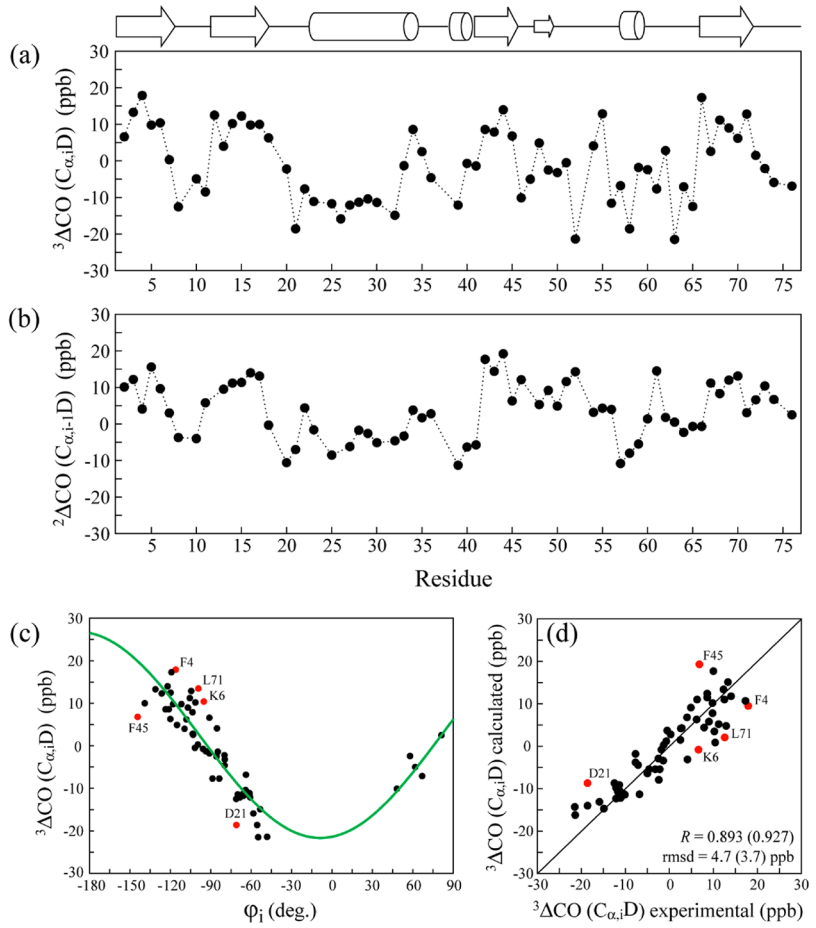

Figure 6. Plots of (a) $^3\Delta CO(C_{\alpha,i}D)$ isotope shifts and (b) $^2\Delta CO(C_{\alpha,i-1}D)$ isotope shifts versus the sequence of ubiquitin; residue numbers correspond to positions of amides that are detected in NMR spectra, while carbonyl shifts of the previous residue (i-1) are reported on the *y*-axis. (c) A plot of $^3\Delta CO(C_{\alpha,i}D)$ shifts as a function of dihedral angle φ of residue i (φ_i) − i.e. the same residue where the $H_\alpha \rightarrow D_\alpha$ substitution occurs. The green curve corresponds to the best-fit functional form of eq 7; (d) a correlation plot showing the agreement between experimentally measured $^3\Delta CO(C_{\alpha,i}D)$ shifts (*x*-axis) and those calculated using eq 7 (*y*-axis) for 60 residues of ubiquitin. Residues shown in red and labeled with residue numbers have the worst agreement with the optimal fit to eq 7. Pearson correlation coefficient *R* and rmsd of the data in (c) are shown with and without (in parentheses) the residues marked in red. Schematic diagram of the secondary structure of ubiquitin is shown above panels (a-b) with arrows and cylinders denoting β-strands and helical regions, respectively.

experimentally, and results in the averaging of the two distinct isotope shifts. Note that the $^3\Delta N(C_{\beta,i}D)$ isotope effects are not resolved in the measurements of $^3\Delta N(C_{\alpha,i-1}D)$ and $^2\Delta N(C_{\alpha,i}D)$ shifts as they have been conducted without the element F_3 (Figure 1). Interestingly, Ile^{13} is the only isoleucine residue in ubiquitin with an eclipsed rotameric state of the $C_\alpha - C_\beta$ bond: $\chi_1 = 126°$ (see also the discussion of possible hydrogen bonding on the shifts of Ile^{13} above).

Two- and Three-Bond Effects on Carbonyl Carbon Chemical Shifts, $^2\Delta CO(C_{\alpha,i-1}D)$ and $^3\Delta CO(C_{\alpha,i}D)$. Three-bond (two-bond) $^{13}CO_{i-1}$ isotope shifts resulting from the $^1H \rightarrow D$ substitutions at $C_{\alpha,i}(C_{\alpha,i-1})$ positions, $^3\Delta CO(C_{\alpha,i}D)(^2\Delta CO(C_{\alpha,i-1}D))$, are measured from the differences in chemical shifts between the $D_{\alpha,i-1}H_{\alpha,i}$ and $D_{\alpha,i-1}D_{\alpha,i}$ ($H_{\alpha,i-1}D_{\alpha,i}$ and $D_{\alpha,i-1}D_{\alpha,i}$) subspectra - see Figure 2c,d (Figure 2b,d) and the examples of peak displacements in Figure 3e (Figure 3f). The $^3\Delta CO(C_{\alpha,i}D)$ and $^2\Delta CO(C_{\alpha,i-1}D)$ shifts are plotted versus the sequence of ubiquitin in Figure 6a and 6b, respectively. The $^3\Delta CO(C_{\alpha,i}D)$ and $^2\Delta CO(C_{\alpha,i-1}D)$ effects are much smaller than their ^{15}N counterparts and vary between −22 (Lys^{63}) and 18 (Phe^4) ppb and −12 (Asp^{39}) and 20 (Ile^{44}) ppb, respectively. A similar qualitative dependence of $^3\Delta CO(C_{\alpha,i}D)$ and $^2\Delta CO(C_{\alpha,i-1}D)$ on the secondary structure can be noted in Figure 6a,b - in fact, $^3\Delta CO(C_{\alpha,i}D)$ and $^2\Delta CO(C_{\alpha,i-1}D)$ shifts are weakly correlated (Pearson $R = 0.65$ for 64 values). The plot of $^3\Delta CO(C_{\alpha,i}D)$ versus dihedral angle ϕ_i (where 'i' is the number of the residue where $H_\alpha \rightarrow D_\alpha$ substitution occurs) that is formed by the three intervening bonds is shown in Figure 6c. Notably, positive $^3\Delta CO(C_{\alpha,i}D)$ values are usually associated with β regions, while negative $^3\Delta CO(C_{\alpha,i}D)$ shifts are observed in helices, turns, and loops (Figure 6a and 6c).

For residues with negative ϕ angles, $^3\Delta CO(C_{\alpha,i}D)$ shifts depend approximately linearly on the value of ϕ (Figure 6c). If the residues with positive ϕ angles are included in the fit, $^3\Delta CO(C_{\alpha,i}D)$ shifts are best-fit to the function, $A + B\cos(\phi_i + C)$, yielding

$$^3\Delta CO(C_{\alpha,i}D)(\text{ppb}) = 2.0 - 23.8\cos(\phi_i + 8°) \quad (7)$$

with rmsd between the measured and back-calculated shifts of 4.7 ppb (Figure 6d; $R = 0.893$; flexible residues Leu^8-Lys^{11} and Leu^{73}-Gly^{76} omitted from the fit) which compares well with the range of measured $^3\Delta CO(C_{\alpha,i}D)$ shifts (40 ppb). Inclusion of other torsion angles (ψ_i or ψ_{i-1}) into the functional form of eq 7 does not lead to statistically significant improvements in the fit.

dx.doi.org/10.1021/jp304300n | J. Phys. Chem. B 2012, 116, 7436−7448

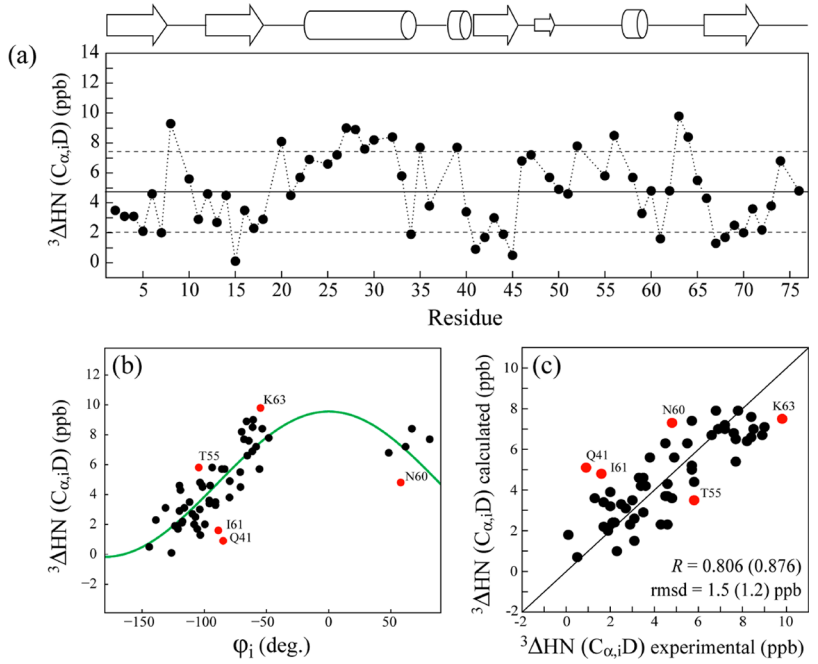

Figure 7. (a) A plot of $^3\Delta$HN($C_{\alpha,i}$D) isotope shifts versus the sequence of ubiquitin; the solid horizontal line corresponds to the mean value of $^3\Delta$HN($C_{\alpha,i}$D), while the dashed horizontal lines are drawn at ±1 standard deviation from the mean; (b) $^3\Delta$HN($C_{\alpha,i}$D) shifts as a function of φ_i dihedral angles. The green curve corresponds to the functional form of eq 8; (c) correlation plot showing the agreement between experimental $^3\Delta$HN($C_{\alpha,i}$D) shifts (*x*-axis) and those predicted from eq 8 (*y*-axis) for 58 amide protons of ubiquitin. Residues showing the worst agreement are shown in red and labeled with residue numbers. Pearson correlation coefficient *R* and rmsd of the data in (c) are shown with and without (in parentheses) the residues marked in red. Schematic diagram of the secondary structure of ubiquitin is shown above the figure, with arrows and cylinders denoting β-strands and helical regions, respectively.

Five amide positions with the largest disagreement between experimental and predicted values of $^3\Delta$CO($C_{\alpha,i}$D) are as follows: Phe,[4] Lys,[6] Asp,[21] Phe,[45] and Leu[71] (Figure 6c,d). Exclusion of these residues from the fit provides the relationship with A = 2.2, B = −24.2, C = 9° and rmsd between the measured and back-calculated values of 3.7 ppb (*R* = 0.927; Figure 6d). Carbonyl oxygens of the residues preceding Phe,[4] Lys,[6] Phe,[45] and Leu[71] participate in strong hydrogen-bonds (≤2.0 Å C═O···HN distances in ubiquitin structure[43]). The values of $^3\Delta$CO($C_{\alpha,i}$D) measured for these residues are higher than predicted from eq 7 with the notable exception of Phe[45] (Figure 6d). Interestingly, anomalous $^2\Delta C_\alpha$(ND) isotope shift has been reported for Phe[45] of ubiquitin earlier[27] and may be related to the fact that this residue is followed by Ala[46] with a positive ϕ angle. Another residue with a very low $^3\Delta$CO($C_{\alpha,i}$D) shift of the preceding carbonyl is Lys[63] (−22 ppb) which is followed by Glu[64] with a positive ϕ angle. The effect of hydrogen bonding on $^3\Delta$CO-($C_{\alpha,i}$D) shifts may be related to the predicted increase in peptide bond planarity upon hydrogen bond formation,[76,77] as suggested above for $^3\Delta$N($C_{\alpha,i-1}$D) effects.

Two-bond $^2\Delta$CO($C_{\alpha,i-1}$D) shifts are only weakly correlated with secondary structure. Although the dependence of $^2\Delta$CO-($C_{\alpha,i-1}$D) isotope shifts on the dihedral angle ψ of the residue where the $H_\alpha \rightarrow D_\alpha$ substitution occurs (ψ_{i-1}, where 'i' is the number of the amide detected in NMR experiments, see Figure 2b,d) is statistically significant and described by the relationship, $^2\Delta$CO($C_{\alpha,i-1}$D) (ppb) = 1.0 + sin(ψ_{i-1}+12°), the pairwise rmsd between the measured and back-calculated $^2\Delta$CO-($C_{\alpha,i-1}$D) is 4.6 ppb (*R* = 0.803 for 60 residues) - a relatively high level of disagreement compared to the range of measured $^2\Delta$CO($C_{\alpha,i-1}$D) shifts (~30 ppb).

Three-Bond Amide Proton Isotope Shifts, $^3\Delta$HN-($C_{\alpha,i}$D). Three-bond ^{1}HN isotope shifts resulting from ^{1}H→D substitutions at $C_{\alpha,i}$ positions, $^3\Delta$HN($C_{\alpha,i}$D), are measured from the differences in ^{1}HN chemical shifts of the $D_{\alpha,i-1}H_{\alpha,i}$ and $D_{\alpha,i-1}D_{\alpha,i}$ molecular species (Figure 2c,d; see examples of peak displacements in Figure 3e). The measured $^3\Delta$HN($C_{\alpha,i}$D) shifts are plotted versus the sequence of ubiquitin in Figure 7a. The $^3\Delta$HN($C_{\alpha,i}$D) effects are very small[14,36,40] and positive varying from ~0 (Leu[15]) to 10 ppb (Lys[63]). The average $^3\Delta$HN($C_{\alpha,i}$D) value is 4.8 ± 2.7 ppb. Notably, higher than average $^3\Delta$HN($C_{\alpha,i}$D) shifts are associated with helical regions, bends, and loops, while smaller than average shifts (~2 to 5 ppb) occur in β-strands (Figure 7a). It is quite remarkable that such small differences in chemical shifts can be quantified in a protein molecule. Selection for the molecular species that are deuterated at $D_{\alpha,i-1}$ positions in the $D_{\alpha,i-1}H_{\alpha,i}$ and $D_{\alpha,i-1}D_{\alpha,i}$ subspectra enables accurate determination of these effects. For example, if both α_i and α_{i-1} sites were protonated ($H_{\alpha,i-1}H_{\alpha,i}$ species selected for in one of the subspectra), the sum of $^3\Delta$HN($C_{\alpha,i}$D) and four-bond $^4\Delta$HN($C_{\alpha,i-1}$D) shifts would be effectively observed. The $^4\Delta$HN($C_{\alpha,i-1}$D) are very small on average and can be measured from the displacements of peaks between the $H_{\alpha,i-1}D_{\alpha,i}$ and $D_{\alpha,i-1}D_{\alpha,i}$ subspectra (estimated average of −1.5 ± 2 ppb; see the histogram of $^4\Delta$HN($C_{\alpha,i-1}$D) values in Figure S6b, Supporting Information), but in some cases may be comparable in magnitude to the $^3\Delta$HN($C_{\alpha,i}$D) effects. Because CH_2 groups in α-sites of glycines cannot be eliminated by the filtering elements F_1 and F_2 in the scheme of Figure 1 as noted above, the measured $^3\Delta$HN($C_{\alpha,i}$D) shifts in the residues following Gly are compromised by an admixture of $^4\Delta$HN($C_{\alpha,i-1}$D) effects. The residues following Gly have been therefore excluded from analysis.

dx.doi.org/10.1021/jp304300n | J. Phys. Chem. B 2012, 116, 7436−7448

The dependence of $^3\Delta HN(C_{\alpha,i}D)$ shifts on the dihedral angle ϕ_i that is formed by the three intervening bonds is shown in Figure 7b. For negative ϕ angles, $^3\Delta HN(C_{\alpha,i}D)$ shifts increase with increasing ϕ_i. If the residues with positive ϕ's are considered, the dependence of $^3\Delta HN(C_{\alpha,i}D)$ on ϕ_i is best described by the simple function, $A + B\cos(\phi_i)$, yielding after least-squares minimization the following relationship

$$^3\Delta HN(C_{\alpha,i}D)\ (\text{ppb}) = 4.7 + 4.9\cos(\phi_i) \quad (8)$$

with rmsd between the measured and back-calculated shifts of 1.5 ppb (Figure 6d; $R = 0.806$; the residues disordered in solution, Leu[8]-Lys[11] and Leu[73]-Gly,[76] and the amides of residues following Gly have been excluded from the fit). Five amide positions with the largest disagreement between experimental and predicted $^3\Delta HN(C_{\alpha,i}D)$ values are as follows: Gln,[41] Thr,[55] Asn,[60] Ile,[61] and Lys[63] (Figure 7b,c). Omission of these residues from the fit provides A = 4.8, B = 5.1, and rmsd between the measured and back-calculated values of 1.2 ppb ($R = 0.867$; Figure 7c). Amide protons of Gln[41] and Asn[60] are hydrogen-bonded to backbone carbonyls of Pro[38] and Ser,[57] respectively, while the amide of Thr[55] is hydrogen bonded to the side-chain carboxyl oxygens of Asp.[58] Amide protons of Ile[61] and Lys[63] are not involved in hydrogen bonds. Apart from the positive ϕ angle of Asn[60] and the fact that Lys[63] is followed by Glu[64] with a positive ϕ angle, there are no unusual features that distinguish these residues and explain why their $^3\Delta HN(C_{\alpha,i}D)$ shifts show larger disagreements with the values predicted by eq 8. We note that the level of agreement achieved between the calculated and predicted $^3\Delta HN(C_{\alpha,i}D)$ shifts in Figure 7c is noticeably inferior to that of ^{15}N and three-bond ^{13}CO isotope shifts described above. This can be related to the small magnitude of the $^3\Delta HN(C_{\alpha,i}D)$ shifts and the lower range of their variability (only ~10 ppb).

Analysis of Measurement Errors and Possible Contributions to Isotope Effects. The small magnitude of the majority of isotope effects considered in this work makes it necessary to estimate the errors in the measurements in relation to statistical deviations of the experimental data from the values predicted from the derived empirical relationships. Although for most of the two- and three-bond isotope effects on ^{15}N, ^{13}CO, and ^1HN backbone nuclei the achieved rmsd's between the measured and back-calculated shifts are approximately an order of magnitude lower that the corresponding ranges of isotope shift variability (~150, 150, 40, and 10 ppb for $^3\Delta N(C_{\alpha,i-1}D)$, $^2\Delta N(C_{\alpha,i}D)$, $^3\Delta CO(C_{\alpha,i}D)$, and $^3\Delta HN(C_{\alpha,i}D)$ shifts, respectively), these deviations exceed several-fold the random uncertainties in the measurements. The respective pairwise rmsd between the shifts obtained in duplicate experiments are 3.0, 3.4, 2.5, and 0.6 ppb for $^3\Delta N(C_{\alpha,i-1}D)$, $^2\Delta N(C_{\alpha,i}D)$, $^3\Delta CO(C_{\alpha,i}D)$, and $^3\Delta HN(C_{\alpha,i}D)$ shifts, implying random uncertainties of the measurements of 2.1, 2.4, 1.8, and 0.4 ppb. These errors are 3-to-10 times lower than the rmsd between experimental and back-calculated shifts in Figures 4d, 5c, 6d, and 7c. Similarly, the estimated random experimental error of 3 ppb for one-bond $^1\Delta C_\alpha(C_{\alpha,i}D)$ shifts is an order of magnitude lower than the rmsd between the measured and back-calculated values (Figure S3b,c; Supporting Information). Clearly, in all the cases, the discrepancies between the measured and predicted isotope shifts cannot be explained by random measurement errors, and the factors affecting deuterium isotope shifts are in play beyond those described by empirical relationships in eqs 4-8. These factors are manifold and may include the following: (i) the effects arising from tertiary (through-space) interactions with other nuclei in a protein structure; (ii) conformation of adjacent residues (i.e., those preceding and following the dipeptide fragments shown in Figure 2); (iii) dependence of isotope shifts on the amino-acid type (i.e., the type of the substituent at carbon-α positions); (iv) hybridization of electronic orbitals; and (v) hydrogen bonding. These effects largely remain poorly understood - especially so for the isotope effects over multiple (>1) bonds. Therefore, the empirical approach followed here provides the simplest practical means for interpretation of isotope effects. Although some attempts have been undertaken to account for putative hydrogen-bonding effects on the isotope shifts in the present study, the importance and the origin of these effects for $^3\Delta N(C_{\alpha,i-1}D)$, $^2\Delta N(C_{\alpha,i}D)$, $^3\Delta CO(C_{\alpha,i}D)$, and $^3\Delta HN(C_{\alpha,i}D)$ shifts remains debatable - unlike in the cases of some multiple-bond, $^n\Delta C(XD)$, isotope shifts[27,30,31,81] and one-bond amide ^{15}N shifts, $^1\Delta N(D)$, in proteins that are predicted to be sensitive to hydrogen bonding by *ab initio* calculations,[32] and trans-hydrogen-bond scalar coupling measurements.[34]

Concluding Remarks. In summary, we described accurate NMR measurements of deuterium isotope effects on the chemical shifts of backbone ^{15}N, ^{13}C, and ^1HN nuclei in proteins arising from ^1H-to-D substitutions at aliphatic carbon sites. Selection for molecular species with defined protonation/deuteration patterns at α and β positions of the polypeptide chain (Figure 2) allows to distinguish and accurately measure deuterium isotope effects on the backbone nuclei removed up to four bonds from the location of the ^1H-to-D replacement. The isotope shifts measured in the partially (~60%) deuterated protein ubiquitin are interpreted in terms of secondary structure via derivation of empirical relationships describing the dependence of isotope shifts on (φ; ψ) dihedral angles of the crystal structure (eqs 4-8).

Because of their relatively large magnitude and strong dependence on the backbone geometry, the two- and three-bond ^{15}N isotope shifts, $^2\Delta N(C_{\alpha,i}D)$ and $^3\Delta N(C_{\alpha,i-1}D)$, are of particular interest. One can envisage their potential utility for NMR structural refinement of small-to-medium size proteins. For example, the described dependence of $^3\Delta N(C_{\alpha,i-1}D)$ shifts on dihedral angle ψ of the previous residue (i-1; eq 5) combined with the dependence of $^2\Delta N(C_{\alpha,i}D)$ on both φ and ψ angles of residue i (eq 6) may be quite restrictive for backbone conformational freedom if $^3\Delta N(C_{\alpha,i-1}D)$ and $^2\Delta N(C_{\alpha,i}D)$ shifts are incorporated together into structure refinement protocols. On the other hand, the measured $^2\Delta N(C_{\alpha,i}D)$ shifts in residues with positive φ angles are considerably smaller than for the rest of the protein molecule (<100 ppb; Figure 5). The readily measured $^2\Delta N(C_{\alpha,i}D)$ isotope effects may therefore serve as a useful diagnostic tool for identification of such residues in proteins. Because of inherent losses in sensitivity of NMR measurements associated with selection of each of the molecular species listed in Figure 2, the described methodology for accurate measurements of deuterium isotope shifts is expected to be limited to small structured protein molecules (up to ~100 residues long) or slightly larger intrinsically disordered proteins, where experimental ^{15}N isotope shifts can be envisaged to restrain the conformational space accessible to the polypeptide chain.

dx.doi.org/10.1021/jp304300n | J. Phys. Chem. B 2012, 116, 7436−7448

■ ASSOCIATED CONTENT

Supporting Information

Figure S1 showing correlation plots of $^{2}\Delta N(C_{\alpha,i}D)$, $^{3}\Delta N(C_{\alpha,i-1}D)$, and $^{3}\Delta CO(C_{\alpha,i}D)$ isotope shifts measured from different combinations of subs-spectra selecting for molecular species protonated/deuterated at α_i/α_{i-1} positions. Figure S2 showing the plots of $^{1}\Delta C_{\alpha}(C_{\alpha,i}D)$ shifts and $^{1}J_{C\alpha\text{-}H\alpha}$ couplings versus the sequence of ubiquitin. Figure S3 showing correlations plots of the measured $^{1}J_{C\alpha\text{-}H\alpha}$ couplings and $^{1}\Delta C_{\alpha}(C_{\alpha,i}D)$ shifts with the values back-calculated from the derived empirical relationships. Figure S4 showing $^{4}\Delta C_{\alpha}(C_{\alpha,i-1}D)$ isotope shifts plotted versus the sequence of ubiquitin. Figure S5 showing a correlation of $^{3}\Delta N(C_{\alpha,i-1}D)$ isotope shifts with amide proton chemical shifts. Figure S6 showing histograms of $^{3}\Delta N(C_{\beta,i}D)$ and $^{4}\Delta HN(C_{\alpha,i-1}D)$ isotope shifts measured in ubiquitin. This material is available free of charge via the Internet at http://pubs.acs.org.

■ AUTHOR INFORMATION

Corresponding Author

*Phone: +1-301-4051504. Fax: +1-301-3140386. E-mail: vitali@umd.edu. Corresponding author address: Biomolecular Sci. Bldg./CBSO, Department of Chemistry and Biochemistry, University of Maryland, College Park, MD 20742, United States.

Notes

The authors declare no competing financial interest.

■ ACKNOWLEDGMENTS

The authors are grateful to Dr. Chenyun Guo (University of Maryland) for preparation of [U-^{15}N; ^{13}C; 60%-^{2}H, 40%-^{1}H]-labeled ubiquitin and Dr. Xinli Liao for the measurement and analysis of $^{1}J_{C\alpha\text{-}H\alpha}$ couplings. V.T. thanks Prof. Rafael Brüschweiler (Florida State University) for useful discussions.

■ REFERENCES

(1) Grzesiek, S.; Anglister, J.; Ren, H.; Bax, A. *J. Am. Chem. Soc.* **1993**, *115*, 4369−70.
(2) Farmer, B. T., II; Venters, R. *J. Am. Chem. Soc.* **1995**, *117*, 4187−8.
(3) Shan, X.; Gardner, K. H.; Muhandiram, D. R.; Rao, N. S.; Arrowsmith, C. H.; Kay, L. E. *J. Am. Chem. Soc.* **1996**, *118*, 6570−9.
(4) Nietlispach, D.; Clowes, R. T.; Broadhurst, R. W.; Ito, Y.; Keeler, J.; Kelly, M.; Ashurst, J.; Oschkinat, H.; Domaille, P. J.; Laue, E. D. *J. Am. Chem. Soc.* **1996**, *118*, 407−15.
(5) Smith, B. O.; Ito, Y.; Raine, A.; Teichmann, S.; Ben-Tovim, L.; Nietlispach, D.; Broadhurst, R. W.; Terada, T.; Kelly, M.; Oschkinat, K.; Shibata, T.; Yokoyama, S.; Laue, E. D. *J. Biomol. NMR* **1996**, *8*, 360−8.
(6) Tugarinov, V.; Hwang, P. M.; Kay, L. E. *Annu. Rev. Biochem.* **2004**, *73*, 107−46.
(7) Pervushin, K.; Riek, R.; Wider, G.; Wüthrich, K. *Proc. Natl. Acad. Sci. U.S.A.* **1997**, *94*, 12366−71.
(8) Gardner, K. H.; Zhang, X.; Gehring, K.; Kay, L. E. *J. Am. Chem. Soc.* **1998**, *120*, 11738−48.
(9) Yang, D.; Kay, L. E. *J. Am. Chem. Soc.* **1999**, *121*, 2571−5.
(10) Fiaux, J.; Bertelsen, E. B.; Horwich, A. L.; Wüthrich, K. *Nature* **2002**, *418*, 207−21.
(11) Tugarinov, V.; Muhandiram, R.; Ayed, A.; Kay, L. E. *J. Am. Chem. Soc.* **2002**, *124*, 10025−35.
(12) Rosen, M. K.; Gardner, K. H.; Willis, R. C.; Parris, W. E.; Pawson, T.; Kay, L. E. *J. Mol. Biol.* **1996**, *263*, 627−36.
(13) Metzler, W. J.; Wittekind, M.; Goldfarb, V.; Mueller, L.; Farmer, B. T. *J. Am. Chem. Soc.* **1996**, *118*, 6800−1.
(14) Gardner, K. H.; Rosen, M. K.; Kay, L. E. *Biochemistry* **1997**, *36*, 1389−401.
(15) Goto, N. K.; Gardner, K. H.; Mueller, G. A.; Willis, R. C.; Kay, L. E. *J. Biomol. NMR* **1999**, *13*, 369−74.
(16) Ruschak, A. M.; Kay, L. E. *J. Biomol. NMR* **2010**, *46*, 75−87.
(17) Hansen, P. E. *Annu. Rep. NMR Spectrosc.* **1983**, *15*, 105−234.
(18) Hansen, P. E. *Prog. NMR Spectrosc.* **1988**, *20*, 207−55.
(19) Reuben, J. *J. Am. Chem. Soc.* **1985**, *107*, 1747−55.
(20) Majerski, Z.; Zuanic, M.; Metelko, B. *J. Am. Chem. Soc.* **1985**, *107*, 1721−6.
(21) Feeney, J.; Partington, P.; Roberts, G. C. K. *J. Magn. Reson.* **1974**, *13*, 268−74.
(22) Hawkes, G. E.; Randall, E. W.; Hall, W. E.; Gattegno, D.; Conti, F. *Biochemistry* **1978**, *17*, 3986−92.
(23) Otter, A.; Liu, X.; Kotovych, G. *J. Magn. Reson.* **1990**, *86*, 657−62.
(24) Kainosho, M.; Nagao, H.; Tsuji, T. *Biochemistry* **1987**, *26*, 1068−75.
(25) Henry, G. D.; Weiner, J. H.; Sykes, B. D. *Biochemistry* **1987**, *26*, 3626−34.
(26) Tüchsen, E.; Hansen, P. E. *Int. J. Biol. Macromol.* **1991**, *13*, 2−8.
(27) Ottiger, M.; Bax, A. *J. Am. Chem. Soc.* **1997**, *119*, 8070−5.
(28) Meissner, A.; Briand, J.; Sørensen, O. W. *J. Biomol. NMR* **1998**, *12*, 339−43.
(29) Meissner, A.; Sørensen, O. W. *J. Magn. Reson.* **1998**, *135*, 547−50.
(30) Takeda, M.; Jee, J.; Ono, A. M.; Terauchi, T.; Kainosho, M. *J. Am. Chem. Soc.* **2009**, *131*, 18556−62.
(31) Takeda, M.; Jee, J.; Terauchi, T.; Kainosho, M. *J. Am. Chem. Soc.* **2010**, *132*, 6254−60.
(32) Abildgaard, J.; Hansen, P. E.; Manalo, M. N.; LiWang, A. *J. Biomol. NMR* **2009**, *44*, 119−26.
(33) Liu, A.; Wang, J.; Lu, Z.; Yao, L.; Li, Y.; Yan, H. *ChemBioChem* **2008**, *9*, 2860−71.
(34) Jaravine, V. A.; Cordier, F.; Grzesiek, S. *J. Biomol. NMR.* **2004**, *29*, 309−18.
(35) Venters, R. A.; Farmer, B. T.; Fierke, C. A.; Spicer, L. D. *J. Mol. Biol.* **1996**, *264*, 1101−16.
(36) Garrett, D.; Seok, Y. J.; Peterkofsky, A.; Clore, G. M.; Gronenborn, A. M. *Biochemistry* **1997**, *36*, 4393−8.
(37) Sheppard, D.; Guo, C.; Tugarinov, V. *J. Am. Chem. Soc.* **2009**, *131*, 1364−5.
(38) Sheppard, D.; Guo, C.; Tugarinov, V. *J. Biomol. NMR* **2009**, *43*, 229−38.
(39) LeMaster, D. M.; LaIuppa, J. C.; Kushlan, D. M. *J. Biomol. NMR* **1994**, *4*, 863−70.
(40) Gardner, K. H.; Kay, L. E. *Annu. Rev. Biophys. Biomol. Struct.* **1998**, *27*, 357−406.
(41) Yashiro, M.; Shigenobu, Y.; Yoshikawa, S. *J. Am. Chem. Soc.* **1986**, *108*, 1096−7.
(42) Aydin, R.; Frankmolle, W.; Schmalz, D.; Günther, H. *Magn. Reson. Chem.* **1988**, *26*, 408−11.
(43) Vijay-Kumar, S.; Bugg, C. E.; Cook, W. J. *J. Mol. Biol.* **1987**, *194*, 531−44.
(44) Shaka, A. J.; Keeler, J.; Frenkiel, T.; Freeman, R. *J. Magn. Reson.* **1983**, *52*, 335−8.
(45) Shaka, A. J.; Lee, C. J.; Pines, A. *J. Magn. Reson.* **1988**, *77*, 274.
(46) Kay, L. E.; Ikura, M.; Tschudin, R.; Bax, A. *J. Magn. Reson.* **1990**, *89*, 496−514.
(47) Geen, H.; Freeman, R. *J. Magn. Reson.* **1991**, *93*, 93−141.
(48) Patt, S. L. *J. Magn. Reson.* **1992**, *96*, 94−102.
(49) Boyd, J.; Soffe, N. *J. Magn. Reson.* **1989**, *85*, 406−13.
(50) Kay, L. E.; Keifer, P.; Saarinen, T. *J. Am. Chem. Soc.* **1992**, *114*, 10663−5.
(51) Schleucher, J.; Sattler, M.; Griesinger, C. *Angew. Chem., Int. Ed. Engl.* **1993**, *32*, 1489−91.
(52) Marion, D.; Ikura, M.; Tschudin, R.; Bax, A. *J. Magn. Reson.* **1989**, *85*, 393.
(53) Zhu, G.; Bax, A. *J. Magn. Reson.* **1990**, *90*, 405−10.

(54) Delaglio, F.; Grzesiek, S.; Vuister, G. W.; Zhu, G.; Pfeifer, J.; Bax, A. *J. Biomol. NMR* **1995**, *6*, 277−93.
(55) Garrett, D. S.; Powers, R.; Gronenborn, A. M.; Clore, G. M. *J. Magn. Reson.* **1991**, *95*, 214−20.
(56) Kontaxis, G.; Clore, G. M.; Bax, A. *J. Magn. Reson.* **2000**, *143*, 184−96.
(57) Fitzkee, N. C.; Bax, A. *J. Biomol. NMR* **2010**, *48*, 65−70.
(58) Tjandra, N.; Bax, A. *J. Magn. Reson.* **1997**, *124*, 512−5.
(59) Ramage, R.; Green, J.; Muir, T. W.; Ogunjobi, O. M.; Love, S.; Shaw, K. *Biochem. J.* **1994**, *299*, 151−8.
(60) Alexeev, D.; Bury, S. M.; Turner, M. A.; Ogunjobi, O. M.; Muir, T. W.; Ramage, R.; Sawyer, L. *Biochem. J.* **1994**, *299*, 159−63.
(61) Cornilescu, G.; Marquardt, J.; Ottiger, M.; Bax, A. *J. Am. Chem. Soc.* **1998**, *120*, 6836−7.
(62) Bax, A.; Ikura, M. *J. Biomol. NMR* **1991**, *1*, 99−104.
(63) Grzesiek, S.; Bax, A. *J. Magn. Reson.* **1992**, *96*, 432−40.
(64) Permi, P. *J. Biomol. NMR* **2002**, *23*, 201−9.
(65) Brutscher, B. *J. Magn. Reson.* **2002**, *156*, 155−9.
(66) Tossavainen, H.; Permi, P. *J. Magn. Reson.* **2004**, *170*, 244−51.
(67) Garbow, J. R.; Weitekamp, D. P.; Pines, A. *Chem. Phys. Lett.* **1982**, *93*, 504−15.
(68) Briand, J.; Sørensen, O. W. *J. Magn. Reson.* **1997**, *125*, 202−6.
(69) Garrett, D. S.; Seok, Y. J.; Liao, D. I.; Peterkofsky, A.; Gronenborn, A. M.; Clore, G. M. *Biochemistry* **1997**, *36*, 2517−30.
(70) Vuister, G. W.; Delaglio, F.; Bax, A. *J. Am. Chem. Soc.* **1992**, *114*, 9674−5.
(71) Ollerenshaw, J. E.; Tugarinov, V.; Skrynnikov, N. R.; Kay, L. E. *J. Biomol. NMR* **2005**, *33*, 25−41.
(72) Tjandra, N.; Feller, S. E.; Pastor, R. W.; Bax, A. *J. Am. Chem. Soc.* **1995**, *117*, 12562−6.
(73) Bevington, P. R.; Robinson, D. K. *Data Reduction and Error Analysis for the Physical Sciences*; WCB/McGraw-Hill: New York, 1992.
(74) Wagner, G.; Pardi, A.; Wüthrich, K. *J. Am. Chem. Soc.* **1983**, *105*, 5948−57.
(75) Hansen, P. E.; Kolonicny, A.; Lycka, A. *Magn. Reson. Chem.* **1992**, *30*, 786−95.
(76) Scheiner, S.; Kern, C. W. *J. Am. Chem. Soc.* **1977**, *99*, 7042−50.
(77) MacArthur, M. W.; Thornton, J. M. *J. Mol. Biol.* **1996**, *264*, 1180−95.
(78) Jurlina, J. L.; Stothers, J. B. *J. Am. Chem. Soc.* **1982**, *104*, 4677−8.
(79) Hu, J. S.; Bax, A. *J. Am. Chem. Soc.* **1997**, *119*, 6360−8.
(80) Berkholz, D. S.; Driggers, C. M.; Shapovalov, M. V.; Dunbrack, R. L. J.; Karplus, P. A. *Proc. Natl. Acad. Sci. U.S.A.* **2012**, *109*, 449−53.
(81) Dziembowska, T.; Hansen, P. E.; Rozwadowski, Z. *Prog. Nucl. Magn. Reson. Spectrosc.* **2004**, *45*, 1−29.